TraMoS. V. Updated ephemeris and multi-epoch monitoring of the hot Jupiters WASP-18Ab, WASP-19b, and WASP-77Ab

Pía Cortés-Zuleta, Patricio Rojo, Songhu Wang, Tobias C. Hinse, Sergio Hoyer, Bastian Sanhueza, Patricio Correa-Amaro, Julio Albornoz

A&A 636, A98 (2020)
https://doi.org/10.1051/0004-6361/201936279

Astronomy & Astrophysics

TraMoS

V. Updated ephemeris and multi-epoch monitoring of the hot Jupiters WASP-18Ab, WASP-19b, and WASP-77Ab*

Pía Cortés-Zuleta[1,2,⋆], Patricio Rojo[1], Songhu Wang[2,⋆⋆], Tobias C. Hinse[3], Sergio Hoyer[4], Bastian Sanhueza[1], Patricio Correa-Amaro[1], and Julio Albornoz[1]

[1] Departamento de Astronomía, Universidad de Chile, Camino El Observatorio 1515, Las Condes, Santiago, Chile
e-mail: pia.cortes@ug.uchile.cl
[2] Department of Astronomy, Yale University, New Haven, CT 06511, USA
[3] Chungnam National University, Department of Astronomy and Space Science, 34134 Daejeon, Republic of Korea
[4] Aix-Marseille Univ., CNRS, CNES, LAM, Marseille, France

Received 9 July 2019 / Accepted 29 January 2020

ABSTRACT

We present 22 new transit observations of the exoplanets WASP-18Ab, WASP-19b, and WASP-77Ab, from the Transit Monitoring in the South project. We simultaneously model our newly collected transit light curves with archival photometry and radial velocity data to obtain refined physical and orbital parameters. We include TESS light curves of the three exoplanets to perform an extended analysis of the variations in their transit mid-time (TTV) and to refine their planetary orbital ephemeris. We did not find significant TTV_{RMS} variations larger than 47, 65, and 86 s for WASP-18Ab, WASP-19b, and WASP-77Ab, respectively. Dynamical simulations were carried out to constrain the masses of a possible perturber. The observed mean square (RMS) could be produced by a perturber body with an upper limit mass of 9, 2.5, 11 and 4 $M_\oplus$ in 1:2, 1:3, 2:1, and 3:1 resonances in the WASP-18Ab system. In the case of WASP-19b, companions with masses up to 0.26, 0.65, 1, and 2.8 $M_\oplus$, in 1:2, 2:1, 3:1, and 5:3 resonances respectively, produce the RMS. For the WASP-77Ab system, this RMS could be produced by a planet with mass in the range of 1.5−9 $M_\oplus$ in 1:2, 1:3, 2:1, 2:3, 3:1, 3:5, or 5:3 resonances. Comparing our results with RV variations, we discard massive companions with 350 $M_\oplus$ in 17:5 resonance for WASP-18Ab, 95 $M_\oplus$ in 4:1 resonance for WASP-19b, and 105 $M_\oplus$ in 5:2 resonance for WASP-77Ab. Finally, using a Lomb-Scargle period search we find no evidence of a periodic trend on our TTV data for the three exoplanets.

Key words. planets and satellites: dynamical evolution and stability – planets and satellites: individual: WASP-77Ab – planets and satellites: individual: WASP-18b – planets and satellites: individual: WASP-19b – planets and satellites: general

1. Introduction

High-precision long-term transit follow-ups provide tremendous opportunities to improve our understanding of exoplanets, allowing us to obtain more accurate measurements of planetary radius, especially for those detected with ground-based transit surveys (e.g., HATNet and HATSouth, Bakos 2012; SuperWASP, Pollacco et al. 2006; KELT, Pepper et al. 2007; TRES, Alonso et al. 2007, CSTAR, Wang et al. 2014). With improved photometry, we can refine planetary orbital ephemeris (Wang et al. 2018a), which is vital to scheduling future transit-related observations, such as those used to measure the Rossiter-Mclaughlin effect (Nutzman et al. 2011; Sanchis-Ojeda & Winn 2011; Sanchis-Ojeda et al. 2013; Wang et al. 2018b) and transmission spectrum follow-up (Mancini et al. 2016a; Mackebrandt et al. 2017).

Long-term photometric follow-up also provides a unique chance to study the variations of the orbital periods. A recent study shows the apparent orbital decay in the WASP-12 system (Patra et al. 2017), which has since inspired a series of theoretical studies (Millholland & Laughlin 2018; Weinberg et al. 2017) to discuss the potential mechanisms. The transit follow-up also plays an important role in the study of the exoplanet system, which shows interesting transit timing variations (TTVs; Ballard et al. 2011; Ford et al. 2012; Steffen et al. 2012a; Fabrycky et al. 2012; Mancini et al. 2016b; Wang et al. 2017a; Wu et al. 2018).

Ballard (2019) predicted that around 5% of planets discovered by TESS (Ricker 2014) will show TTVs. Transit follow-up of these targets is critical because most of them will only be monitored for ∼27 days, whereas the typical TTV period is in years. Furthermore, extended TTV studies are crucial to confirm or rule out exoplanetary systems, in cases where space-based observations will not cover the long timescales required to characterize them (von Essen et al. 2018). Therefore, combining ground- and space-based observations will be crucial.

The TTV method (Miralda-Escudé 2002; Agol et al. 2005; Holman & Murray 2005) also provides a powerful tool to detect additional low-mass planets in hot Jupiter systems, which are usually hard to find using other techniques (Steffen et al. 2012b). Many efforts have been devoted to this field (Pál et al. 2011; Hoyer et al. 2012, 2013; Szabó et al. 2013), but so far only two hot Jupiters have been found to be accompanied by additional close-in planets (WASP-47: Becker et al. 2015, and Kepler-730: Cañas et al. 2019). The accurate occurrence rate of the "WASP-47-like" system, which hosts a hot Jupiter and at least one additional planet with a period of less than 100 days, is still unknown.

⋆ Photometry tables (full Table 2) are available at the CDS via anonymous ftp to cdsarc.u-strasbg.fr (130.79.128.5) or via http://cdsarc.u-strasbg.fr/viz-bin/cat/J/A+A/636/A98
⋆ LSSTC DSFP Fellow.
⋆⋆ 51 Pegasi b Fellow.

To refine orbital parameters of currently known exoplanets, and to search for additional planets using the TTV method, we organized the Transit Monitoring in the South hemisphere (TraMoS) project (Hoyer et al. 2011) which began in 2008. We use one-meter-class telescopes in the north of Chile to conduct high-precision long-term transit follow-up.

Following the previous efforts from the TraMoS project, in this work, we present new light curves of three hot Jupiters: WASP-18Ab, WASP-19b, and WASP-77Ab. Combining our new light curves, and archival photometric and radial velocity data sets, we refined the orbital and physical parameters of the systems and constrained the upper mass limit of potential additional planetary companions.

WASP-18Ab is a transiting hot Jupiter discovered by Hellier et al. (2009) within the WASP-South transit survey (Pollacco et al. 2006). It is an extremely close-in planet with an orbital period of 0.94 days. The host star is an F6 type and is the brightest component of a binary system (Csizmadia et al. 2019; Fontanive et al. 2019). Regarding its physical properties, WASP-18Ab is about ten times more massive than Jupiter with approximately the same radius ($M_{\rm P} = 10.3\,M_{\rm Jupiter}$, $R_{\rm P} = 1.1\,R_{\rm Jupiter}$). Even though a rapid orbital decay was predicted theoretically (Hellier et al. 2009), it is not yet observed (Wilkins et al. 2017) and new theoretical models propose a variation of fewer than 4 s in the transit time over a baseline of 20 yr (Collier Cameron & Jardine 2018).

The hot Jupiter WASP-19b was first reported by Hebb et al. (2010). This exoplanet has one of the shortest orbital periods ever discovered ($P = 0.788$ days). With a mass of $1.15\,M_{\rm Jupiter}$ and a radius of $1.31\,R_{\rm Jupiter}$, the planet orbits an active G8 dwarf.

The third exoplanet we followed-up in this work was first presented by Maxted et al. (2013a); WASP-77Ab has a mass of $1.8\,M_{\rm Jupiter}$ and a radius of $1.2\,R_{\rm Jupiter}$. It transits a G8 star in 1.36 days, which is the brightest component of a visual binary system. This system has a separation of 3.3 arcsec.

This paper is organized as follows. In Sect. 2 we summarize the photometric observations and their reduction process. In Sect. 3 we present the new light curves of the targets and the description of the technique used to obtain their orbital and physical parameters. The principal results and their consequences are presented in Sect. 4. Finally, a summary and conclusions are described in Sect. 5.

2. Observations and data reduction

We collected eight light curves for WASP-18Ab between 2009 and 2017, nine light curves for WASP-19b between 2011 and 2017, and five light curves for WASP-77Ab between 2015 and 2017. We included four transits of WASP-77Ab from the Exoplanet Transit Database (ETD: Poddaný et al. 2010) to cover a larger time span.

All the photometry was collected using either the Danish 1.54 m telescope at ESO La Silla Observatory or the SMARTS 1 m at Cerro Tololo Observatory (CTIO), except for one transit of WASP-77Ab that was observed with the Warsaw 1.3 m at Las Campanas Observatory (LCO). The log of our observations is in Table 1. The new TraMoS light curves used for this work are presented in Fig. 1 and examples of the photometry are listed in Table 2.

For the photometric observations conducted on the Danish telescope, we used the Danish Faint Object Spectrograph and Camera (DFOSC) instrument, which has a $2\mathrm{K} \times 2\mathrm{K}$ CCD with a 13.7×13.7 arcmin^2 field of view (FoV) and a pixel scale of $0.39''$ per pixel. To reduce the readout time, some of the Danish 1.54 m images were windowed to only include the target star and its closest reference stars. The observations of the transits of WASP-18Ab during 2016 and 2017 were forced to be windowed due to a malfunction of the CCD. For those transits, only one reference star was used to perform the photometry.

The SMARTS 1 m has the Y4KCam instrument which is a $4\mathrm{K} \times 4\mathrm{K}$ CCD camera with a 20×20 arcmin^2 FoV and a pixel scale of $0.289''$ per pixel.

For the observation with the Warsaw 1.3 m telescope, we used a 2048×4096 CCD camera chip with a 1.4 square degrees of FoV and $0.26''$ per pixel scale. No windowing or binning was used during the observations on both SMARTS 1 m and the Warsaw 1.3 m telescope.

As suggested by Southworth et al. (2009), most of our observations used the defocus technique, specifically those conducted after 2011. This allows longer exposure times on bright targets and improves the photometric precision. We adjusted the exposure time during the observations if the weather was not ideal. The recorded Julian dates in the coordinated universal time ($\mathrm{JD_{UTC}}$) were converted into barycentric Julian dates in the barycentric dynamical time standard ($\mathrm{BJD_{TDB}}$) following the procedure as in Eastman et al. (2010).

We reduced the data by using our custom pipeline. It follows the standard procedures of reduction, calibration, and aperture photometry, but customized for each used instrument. The data were bias and flat-field calibrated using master bias and master flat-field images. These master images were built from at least ten individual bias and flats obtained at the beginning of each observing night. When that was not possible, we used bias and flat-field images from the closest observing night. The flux time series of all the selected stars in the FoV was then obtained using aperture photometry. The radius of the aperture was chosen to minimize the dispersion of the light curve in the out-of-transit points. To remove the sky-background we used the median of the pixels in a ring around the star. The size of this ring depends on each case, but it was determined in an iterative process over a range of values for external and internal sky radius. To built the relative photometry of the target we use the best reference stars in terms of their variability after checking for saturation and stability. The pipeline semi-automatically finds the best aperture and the size of the ring for the sky that produces the light curve with the lowest root mean square (RMS).

3. Light-curve and RV analysis

To obtain the refined orbital and physical parameters of WASP-18Ab, WASP-19b, and WASP-77Ab, as well as their transit mid-time ($T_{\rm c}$), we used EXOFASTv2 (Eastman et al. 2013; Eastman 2017) to model the light curves together with archived RV data from Hellier et al. (2009), Hebb et al. (2010), and Maxted et al. (2013a).

EXOFASTv2 is an Interactive Data Language (IDL) code designed to simultaneously fit transits and radial-velocity measurements obtained from different filters or different telescopes. It uses the differential evolution Markov chain Monte Carlo (DE-MCMC) method to derive the values and their uncertainties of the stellar, orbital, and physical parameters of the system.

The stellar parameters of WASP-18A, WASP-19, and WASP-77A were computed using the MESA Isochrones and Stellar Tracks (MIST) model (Dotter 2016) included in EXOFASTv2. We applied Gaussian priors in surface gravity $\log g$, effective temperature $T_{\rm eff}$, and metallicity [Fe/H] of the stars from Hellier et al. (2009), Hebb et al. (2010) and Maxted et al. (2013a) for WASP-18A, WASP-19, and WASP-77A, respectively. These

Table 1. Log of observations.

Target	Date (UTC)	Epoch [a]	Telescope	Filter	N [b]	T_{exp} [c] (sec)	airmass	*FWHM* (arcsec)	RMS [d] (mmag)
WASP-18	2009 Oct. 28	−1904	SMARTS 1 m	*I*	1412	1.5	1.3 → 1.0 → 1.7	1.18	8.49
	2009 Oct. 29	−1903	SMARTS 1 m	*I*	1435	2	1.4 → 1.0 → 1.6	1.59	5.67
	2009 Oct. 30	−1902	SMARTS 1 m	*I*	1198	2	1.2 → 1.0 → 1.6	1.93	4.50
	2011 Sep. 06	−1184	SMARTS 1 m	*I*	203	15	2.1 → 1.6 → 1.3	5.66	2.40
	2016 Sep. 24 [e]	776	Danish 1.54 m	*I*	138	90	1.0 → 1.2 → 1.5	16.22	1.05
	2016 Sep. 25 [e]	777	Danish 1.54 m	*I*	159	90	1.0 → 1.2 → 1.5	17.55	0.96
	2016 Sep. 26 [e]	778	Danish 1.54 m	*I*	113	90	1.2 → 1.0 → 1.1	17.94	0.87
	2017 Sep. 29 [e]	1169	Danish 1.54 m	*R*	330	30	1.0 → 1.3 → 1.5	18.60	2.53
WASP-19	2011 Apr. 22	−923	SMARTS 1 m	*I*	626	12	1.0 → 1.4 → 1.9	0.72	4.31
	2011 Dec. 24	−611	SMARTS 1 m	*I*	364	18	1.6 → 1.3 → 1.1	1.42	35.9
	2013 Mar. 13	−47	Danish 1.54 m	*R*	336	35	1.3 → 1.1 → 1.2	6.82	2.15
	2013 Apr. 20	1	Danish 1.54 m	*R*	153	100	1.1 → 1.0 → 1.3	8.46	0.80
	2015 Mar. 04	867	Danish 1.54 m	*R*	235	60	1.3 → 1.0 → 1.2	3.99	0.84
	2016 Apr. 14	1383	Danish 1.54 m	*I*	87	100	1.0 → 1.3 → 1.6	4.56	0.71
	2017 Feb. 14	1771	Danish 1.54 m	*I*	137	90	1.1 → 1.0 → 1.3	4.21	0.79
	2017 Apr. 08	1838	Danish 1.54 m	*R*	125	90	1.1 → 1.0 → 1.2	3.87	0.81
	2017 Oct. 03	2064	Danish 1.54 m	*R*	43	110	3.0 → 2.4 → 1.8	3.08	1.70
WASP-77	2013 Aug. 20	−659	ETD [f]	clear	103	120	2.5 → 2.0 → 1.4	- [g]	3.87
	2013 Oct. 30	−606	ETD [f]	clear	690	12	1.7 → 1.5 → 1.6	- [g]	5.91
	2015 Sep. 29	−92	Danish 1.54 m	*R*	244	30	1.2 → 1.1 → 1.3	10.99	0.84
	2015 Oct. 03	−89	Danish 1.54 m	*R*	138	60	1.1 → 1.4 → 1.7	12.09	1.84
	2016 Sep. 26	175	Danish 1.54 m	*I*	90	90	1.1 → 1.3 → 1.6	19.50	0.47
	2016 Sep. 30	177	ETD [f]	clear	66	180	1.5 → 1.4 → 1.8	- [g]	2.74
	2016 Oct. 07	183	Warsaw 1.3 m	*I*	237	60	1.4 → 1.1 → 1.3	8.32	2.38
	2016 Dec. 09	229	ETD [f]	*R*	57	180	2.4 → 2.0 → 1.4	7.50	2.11
	2017 Oct. 01	447	Danish 1.54 m	*B*	224	30	1.2 → 1.1 → 1.4	2.06	3.48

Notes. [a]The epoch 0 is T_0 in Tables A.1, A.2, and A.3, for WASP-18Ab, WASP-19b, and WASP-77Ab, respectively. [b]Number of observations. [c]Exposure time of each observation. For the variable exposure times, we consider the average during the night. [d]The RMS values were computed from the best fitted model of each light curve. [e]Light curves computed with only one reference star. [f]Light curves obtained from the Exoplanet Transit Database (ETD; `https://var2.astro.cz/ETD`). [g]Information not provided.

priors have mixed origins. While the priors used in WASP-18A came from stellar evolutionary tracks models, for WASP-19 and WASP-77A their priors have a spectroscopic origin.

We were not able to separate the contribution of the two companions of the binary system WASP-77. The separation of the components is 3.3 arcsec, but our photometry aperture is about 10 arcsec. Therefore, we computed the dilution factor – fraction of the light that comes from the companion star – for each filter of our data set to get the real transit depth of WASP-77Ab. Because of the lack of good-quality magnitude measurements for the fainter companion WASP-77B in the *B*, *I*, *R* and clear passbands, we derived them from the *Gaia* magnitude (G = 11.8356) assuming black-body radiation. The derived magnitudes for WASP-77B are V = 11.97, B = 12.72, R = 11.57, I = 10.95, and clear = 11.78.

We set previously published values as uniform priors for the DE-MCMC in all the transit and RV parameters, and the quadratic limb darkening coefficients and T_c. The priors were taken from the discovery papers of WASP-18Ab (Hellier et al. 2009), WASP-19b (Hebb et al. 2010), and WASP-77Ab (Maxted et al. 2013a).

To significantly reduce the convergence time of the chains during the EXOFASTv2 fitting, we started from shorter chains. Thus, the total time to complete that run is reduced. After it finished, we took the values from its best model and used them as priors for the next short run. This process was repeated until the chains were converged and well-mixed. The best-fitted model is presented in Fig. 1 for our transit data from the TraMoS project, and in Fig. 2 for the RV archival data. In Fig. 3, the light curves were phase folded for clarity and overplotted in color are the best-fitted models.

4. Results and discussion

4.1. Transit parameters and physical properties

4.1.1. WASP-18Ab

The resulting parameters from the global fit of the WASP-18A system in comparison with the results of the discovery paper Hellier et al. (2009) and the most recent analysis with TESS data (Shporer et al. 2019) are listed in Table A.1. While in Hellier et al. (2009) the analysis was performed combining photometry and RV data, in Shporer et al. (2019) only photometric data were used.

As the stellar spectroscopic priors were taken from the discovery paper Hellier et al. (2009), our results for the stellar mass M_* and radius R_* agree with theirs, as expected, as well as the rest of the stellar parameters. Shporer et al. (2019) does not present results of stellar parameters.

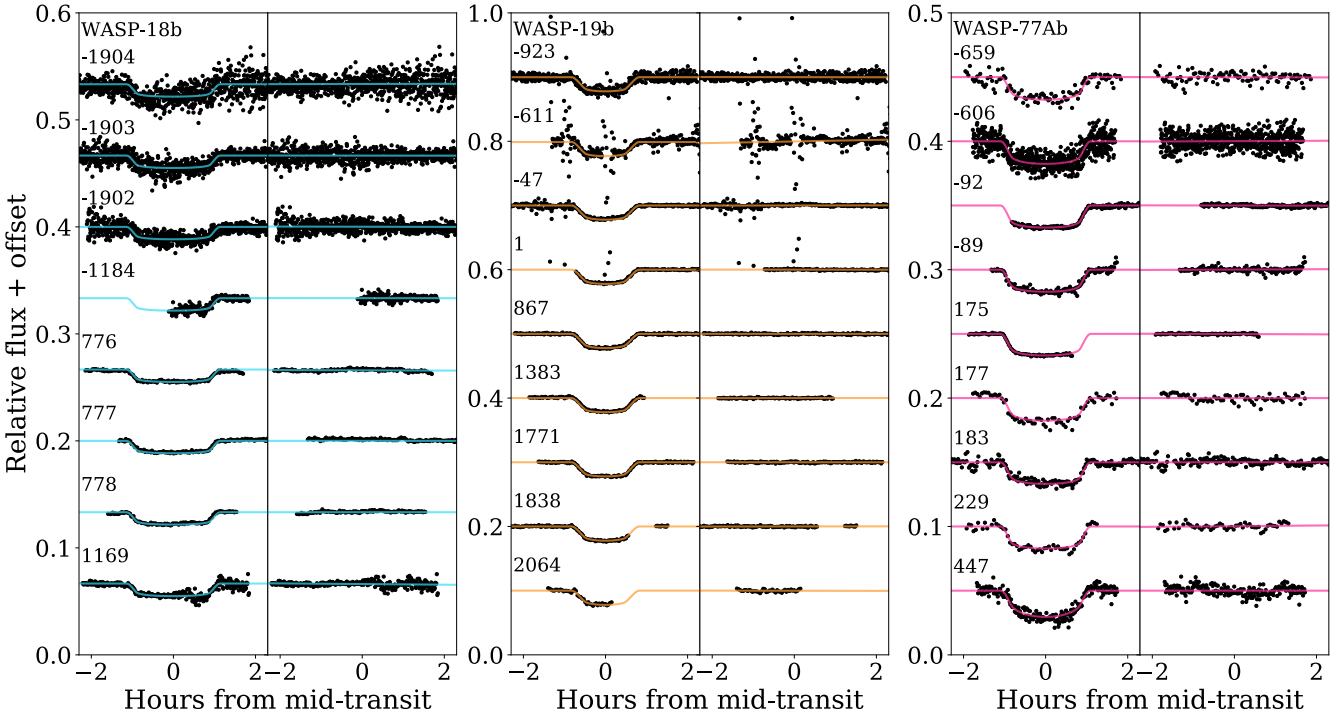

Fig. 1. Light curves from the TraMoS project of WASP-18A, WASP19 and, WASP77A during eight, nine, and nine different transits, respectively. The best-fit model from EXOFASTv2 is shown as a light blue solid line for WASP-18Ab, orange for WASP-19b, and pink for WASP-77Ab. On the right of each panel are the corresponding residuals of the model. For clarity, both light curves and their residuals are offset artificially. The epoch number is indicated above each light curve. Technical information about each observation is listed in Table 1.

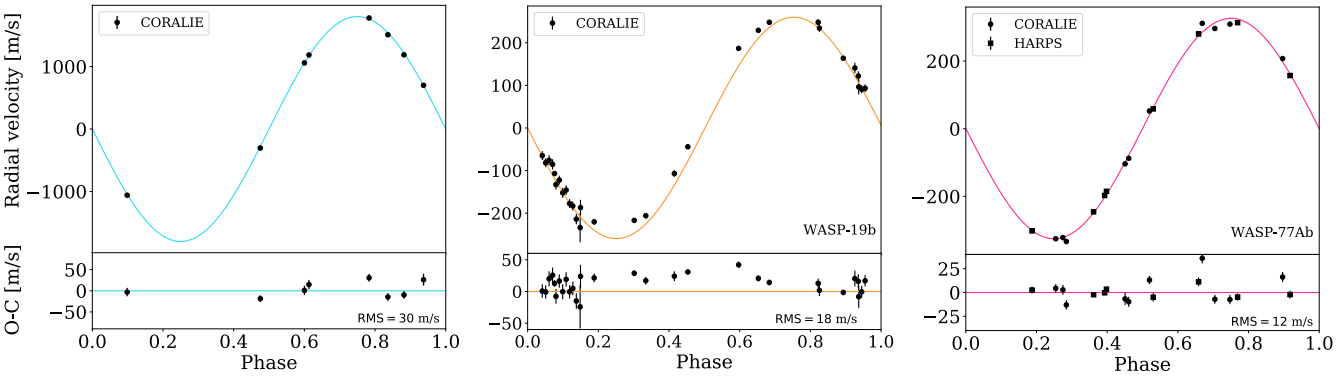

Fig. 2. Radial-velocity observations of WASP-18A, WASP-19, and WASP-77A from Hellier et al. (2009), Hebb et al. (2010), and Maxted et al. (2013a), respectively. The best-fit model from the joint modeling of RV and light curves with EXOFASTv2 is shown as a solid colored line: light blue for WASP-18Ab, orange for WASP-19b, and pink for WASP-77Ab. The residuals of the model are shown in the *bottom panel* of each figure.

In the case of the primary transit parameters, the greatest difference is found in the radius of the planet in stellar radii R_p/R_*. Our reported R_p/R_* is 7.5σ and 4.1σ larger that the reported by Hellier et al. (2009) on the discovery paper and the recent result from Shporer et al. (2019), respectively. Our transit duration T_{14} is also 3.8σ larger than the value from Hellier et al. (2009). For the radial velocity parameters, the RV semi-amplitude derived from our analysis is consistent with the value of Hellier et al. (2009) because the same data were used.

Finally, the derived parameters of the system are, in general, in good accordance with the values from Hellier et al. (2009) and Shporer et al. (2019). Although our value for the eccentricity e is within 1σ of the result from Hellier et al. (2009), it is important to highlight that the difference may be a consequence of our limited number of RV measurements. We did not consider one RV measurement from Hellier et al. (2009) taken during a transit event.

4.1.2. WASP-19b

The results of the global fit of the WASP-19 system are listed in Table A.2, in comparison with the previous values from the discovery paper (Hebb et al. 2010) and a more recent work (Lendl et al. 2013).

To estimate the stellar parameters of WASP-19, we used the stellar spectroscopic parameters from Hebb et al. (2010) as priors. Thus, in general, our results agree with those from the discovery paper. The most important discrepancies are the density of the star ρ_* and the surface gravity $\log g$, showing +2.5σ and −3.2σ difference, respectively. Our results are all in good

Table 2. Example photometry of WASP-18A, WASP-19, and WASP-77A.

Target	BJD_{TDB} [(a)]	Relative flux	Error
WASP-18A	2 457 658.658241	1.00168	0.00078
	2 457 658.660591	1.00138	0.00080
	2 457 658.661771	1.00195	0.00082
	2 457 658.662940	1.00261	0.00085
	2 457 658.664109	1.00137	0.00086
	...	...	...
WASP-19	2 457 086.543926	1.00099	0.00086
	2 457 086.544916	1.00173	0.00091
	2 457 086.545905	1.00139	0.00086
	2 457 086.546895	1.00045	0.00094
	2 457 086.547886	1.00064	0.00093
	...	...	...
WASP-77A	2 457 299.78624	1.00229	0.00028
	2 457 299.78764	1.00116	0.00022
	2 457 299.78855	1.00201	0.00022
	2 457 299.78946	1.00216	0.00022
	2 457 299.79092	1.00133	0.00021
	...	...	...

Notes. These tables are available at the CDS. [(a)]The column time was converted to (BJD_{TDB}), following the procedure of Eastman et al. (2010).

agreement with those of Lendl et al. (2013). The stellar surface gravity $\log g$ derived from spectroscopy may be different from the values that include constraints from transit data (Torres et al. 2012).

For values of the primary transit parameters obtained from the light curves, the greatest differences are found in the orbital inclination i and the total transit duration T_{14}. We report an inclination value 5.1σ smaller than that of Hebb et al. (2010), but ours agrees with the estimate of Lendl et al. (2013). On the other hand, our estimation of T_{14} is significantly greater than that of Hebb et al. (2010) by 9σ, but the difference is only by 3.5σ when compared with Lendl et al. (2013). We also report a more precise impact parameter b and transit depth δ.

As the same RV data set from the discovery paper (Hebb et al. 2010) was used to perform our analysis, the almost identical values in the RV semi-amplitude K are not surprising. Moreover, the values from Lendl et al. (2013) are also in agreement.

The planetary parameters derived from the light curve and radial velocity analysis almost all agree with the comparison studies. The only parameter with a difference greater than 3σ is our estimation of the equilibrium temperature T_{eq} compared with the result of Hebb et al. (2010). However, our result is in better agreement with Lendl et al. (2013), differing by less than 2σ.

4.1.3. WASP-77Ab

Table A.3 lists the results of the global fit of the WASP-77A system using photometry and RV data in comparison with the values from its discovery paper (Maxted et al. 2013a). No other previous study has reported bulk measurements for this system.

Almost all the stellar parameters agree with (Maxted et al. 2013a), except for a -9.7σ difference in the stellar surface gravity $\log g$, where our reported value is more precise. This difference can be explained in a similar manner to the difference in surface gravity found for WASP-19 (see Sect. 4.2.1).

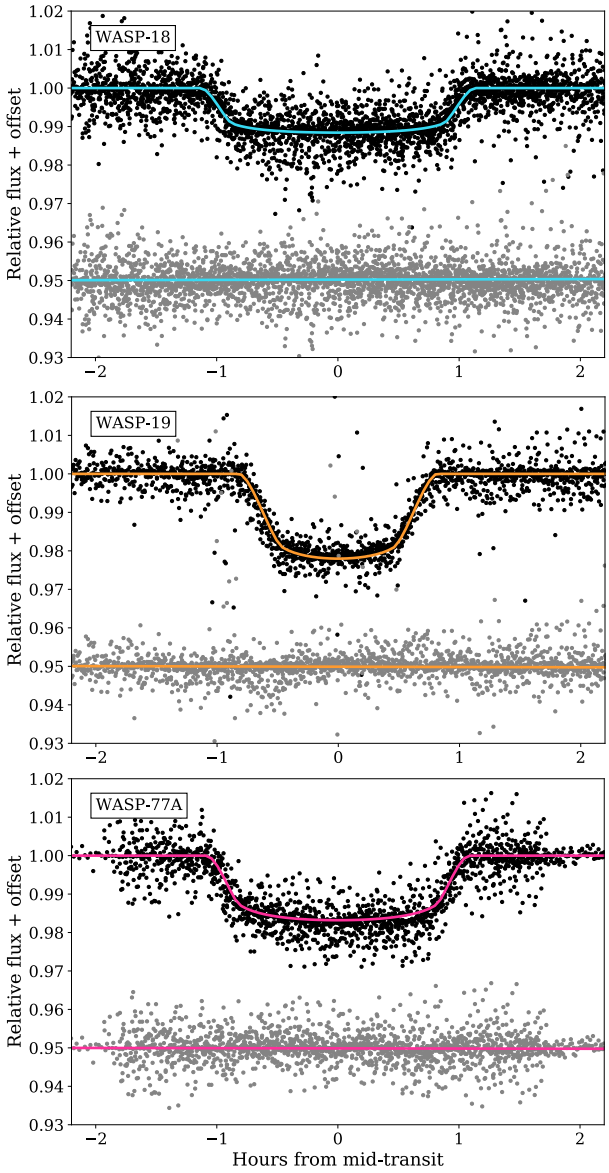

Fig. 3. Phased light curves of WASP-18Ab, WASP-19b, and WASP-77Ab transits. The three data set of light curves are fitted simultaneously with RV archival data using EXOFASTv2 in order to estimate the orbital and physical parameters of the system. *Top panel*: the light blue solid line shows the best-fit model for WASP-18Ab, and below are the residuals in gray. The same is shown for WASP-19b in orange (*center panel*), and for WASP-77Ab in pink (*bottom panel*).

The primary transit parameters, as well as the RV parameters and the derived planetary parameters, are consistent with the results from Maxted et al. (2013a).

4.2. Transit timing variations

A transit timing variation (TTV) is represented by the difference in time between the expected transit mid-time assuming a Keplerian motion for the planet, and the observed transit mid-time. The TTVs for the three targets were computed considering our transit mid-times from the TraMoS project, as well as including previous transit mid-times already published and new transit mid-times coming from TESS (Ricker 2014) light curves.

During its first year, TESS observed stars exclusively in the southern hemisphere. WASP-18A was observed during Sectors 2

and 3 producing 45 complete transit events. WASP-19 was observed in Sector 9 producing 29 complete transit events, and WASP-77A was observed during Sector 4 and produced 15 complete light curves.

TESS data are reduced by the Science Processing Operations Center (SPOC) and after being processed, they are archived in the Mikulski Archive for Space Telescopes (MAST[1]) catalog where they can be downloaded directly by anyone. We downloaded the complete light curves of our three targets from the MAST catalog. The transit events were then identified and cut into independent light curves. For each TESS light curve, its corresponding transit mid-time T_c was computed using EXOFASTv2 (Eastman et al. 2013). The transit mid-times of all the new TESS light curves are listed in Tables A.4, A.5, and A.6.

A refined orbital period was linearly fitted, considering a total of 63 transit mid-times of WASP-18Ab, 88 of WASP-19, and 26 of WASP-77Ab. Along with the linear model, we also tested a second-degree polynomial to analyze a possible orbital decay. Both models considered the errors of the data. Figure 4 presents all the TTV measurements for the transit mid-times of WASP-18Ab, WASP-19b, and WASP-77Ab.

If the planet stays in a Keplerian orbit, its transit mid-time T_c of each epoch E should follow a linear function of the orbital period P:

$$T_c(E) = T_c(0) + E \cdot P, \quad (1)$$

where $T_c(0)$ is the optimal transit time in an arbitrary zero epoch. The best-fit values of $T_c(0)$ for WASP-18Ab, WASP-19b, and WASP-77Ab are listed in Tables A.1, A.2, and A.3, respectively.

4.2.1. WASP-18Ab

For this system, the proposed linear ephemeris equation considering 63 transit mid-times is:

$$T_c(E) = 2456926.27460 \pm (94) + E \cdot 0.941452417 \pm (27). \quad (2)$$

Table A.4 lists the transit mid-times and their deviation from the proposed linear ephemeris (TTV) of TraMoS data, previous published works (Triaud et al. 2010; Hellier et al. 2009; Maxted et al. 2013b) and TESS light curves of WASP-18Ab.

The top panel of Fig. 4 is the linear plot of TTV versus epoch for this planet. The deviations of the transit mid-times from the linear ephemeris has an RMS of 47 s. The greater deviations come from the transit mid-time of the epochs −1904 and −1184, which are over the linear ephemeris by 2.1σ. If those values are removed, the RMS decreases to 35 s. The TTVs listed in Table A.4 lie within 1.5σ of the linear fit, except for epochs −1904 and −1184. Epoch −1184 has the greatest error in our sample because it is not a complete transit, while epoch −1904, the one with the highest deviation from the linear ephemeris on our sample, was observed during suboptimal weather conditions.

When testing the goodness of the linear fit, $\chi^2_{red} = 0.36$, while for a second-degree polynomial $\chi^2_{red} = 0.35$, and therefore an orbital decay can be discarded in accordance with theoretical estimations (Collier Cameron & Jardine 2018).

4.2.2. WASP-19b

The proposed equation for linear ephemeris, considering 88 transit times of WASP-19b is:

$$T_c(E) = 2456402.7128 \pm (16) + E \cdot 0.788838940 \pm (30). \quad (3)$$

[1] https://exo.mast.stsci.edu/

The TTV values from the proposed linear ephemeris are listed in Table A.5, including transit mid-times from TraMoS, TESS and previous studies of WASP-19b (Hebb et al. 2010; Anderson et al. 2010; Lendl et al. 2013; Tregloan-Reed et al. 2013; Bean et al. 2013; Mancini et al. 2013). Some of the transit mid-times from Mancini et al. (2013) come from the Exoplanet Transit Database catalog and they are accordingly identified in Table A.5.

The middle panel of Fig. 4 shows the TTV values versus epoch for all the transit times considered in this work. The RMS from the linear ephemeris is about 65 s. Epochs −1311, −1011, −886, and −642 show a deviation of more than 3σ from the linear ephemeris. If these deviations are removed, then the RMS decreases to 52 s. Moreover, in our data, epoch −611 has one of the greatest errors because of poor weather conditions.

Considering all the transit mid-times from Table A.5, the linear fit shows $\chi^2_{red} = 0.65$. A second-degree polynomial was also tested to reject or not a possible orbital decay. The goodness of that fit is $\chi^2_{red} = 0.64$.

4.2.3. WASP-77Ab

As in the previous targets, we computed a refined linear ephemeris equation for WASP-77A considering 26 transit times:

$$T_c(E) = 2457420.88439 \pm (85) + E \cdot 1.36002866 \pm (17). \quad (4)$$

Table A.3 lists the TTV values of our transit times (TraMoS) and those of the transit times from previous works (Turner et al. 2016; Maxted et al. 2013a) and TESS. At the bottom of Fig. 4, the TTV of WASP-77Ab is plotted versus epoch. The scatter of all the transit times is about RMS = 86 s.

Epochs 175 and 229 are respectively 2.3 and 3σ above the expected transit time following the linear ephemeris. The remaining epochs lie within 1.5σ of their expected transit time. When epochs 175 and 229 are removed, the RMS decreases to 66 s.

Considering all the transit times, the linear fit has $\chi^2_{red} = 1.03$, and the second-degree polynomial has $\chi^2_{red} = 0.72$. Nevertheless, the second-order fit is highly dominated by the outlier at epoch 229 (see Fig. 4). After removing this latter outlier, the reduced chi-squared is $\chi^2_{red} = 0.37$. In all cases, the best fit corresponds to the linear ephemeris. The variation in the transit mid-time at epoch 229 may be caused by suboptimal weather conditions (100% humidity) during the observation and the lack of good coverage in the after-transit baseline.

4.3. Upper mass limits of a hypothetical perturber

The results from our mid-transit-time study (see Sect. 4.2) allow us to infer an upper mass limit for an additional planet in each system. A perturbing planet will introduce a change in the mid-transit times of a known planet, which can be quantified by the RMS scatter around the nominal (unperturbed) linear ephemeris. The TTV effect is amplified for orbital configurations involving mean-motion resonances (Agol et al. 2005; Holman & Murray 2005; Nesvorný & Morbidelli 2008). In principle, this amplification should allow the detection of a low-mass planetary perturbing body. A larger perturbation implies a larger RMS scatter around the nominal ephemeris.

The applied method follows the technique described in Wang et al. (2018a, 2017b, 2018c). The calculation of an upper mass limit is performed numerically via direct orbit integrations. For this task, we modified the FORTRAN-based

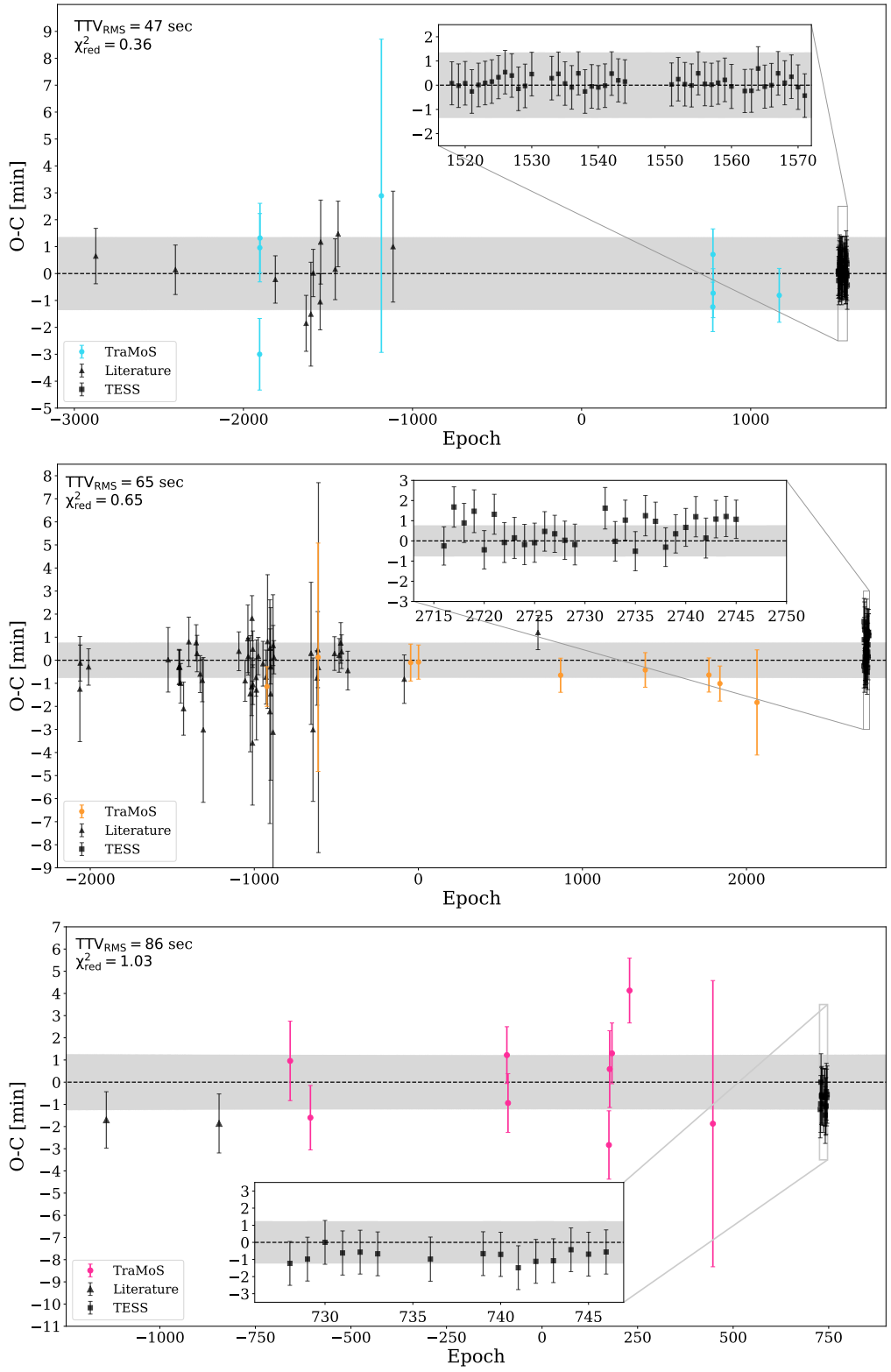

Fig. 4. Observed minus calculated transit mid-times (TTV) for WASP-18Ab (*top panel*), WASP-19b (*center panel*), and WASP-77Ab (*bottom panel*). The dashed black line corresponds to the proposed linear ephemeris, i.e., zero deviation from the predicted transit mid-time (see Sect. 4.2) computed from our refined orbital period. For that, we considered 63, 88, and 26 transit times of WASP-18Ab, WASP-19b, and WASP-77Ab, respectively. The gray area corresponds to the error propagation at 1σ, where the quadratic trend appears almost horizontal. The circles in color are the TTVs from the new light curves of the TraMoS project (WASP-18Ab: light blue, WASP-19b: orange, WASP-77Ab: pink). In black are TTVs measured from different sources of transit mid-time data: the triangles are previously published transit mid-times and the squares are TESS data. The RMS scatter from the linear ephemeris are 47 s for WASP-18Ab; 65 s for WASP-19b, and 86 s for WASP-77Ab.

MICROFARM[2] package (Goździewski 2003; Goździewski et al. 2008) which uses OPENMPI[3] to spawn hundreds of single-task parallel jobs on a suitable super-computing facility. The package's main purpose is the numerical computation of the Mean Exponential Growth factor of Nearby Orbits (Cincotta & Simó 2000; Goździewski et al. 2001; Cincotta et al. 2003, MEGNO) over a grid of initial values of orbital parameters for an n-body problem. The calculation of the RMS scatter of TTVs in the present work follows a direct brute-force method, which proved to be robust given the availability of computing power.

Within the framework of the three-body problem, we integrated the orbits of one of our three hot Jupiters and an additional perturbing planet around their host stars. The mid-transit time was calculated iteratively to a high precision from a series of back-and-forth integrations once a transit of the transiting planet was detected. The best-fit radii of both the planet and the host star were accounted for. We then calculated an analytic least-squares regression to the time-series of transit numbers and mid-transit times to determine a best-fitting linear ephemeris with an associated RMS statistic for the TTVs. The RMS statistic was based on a twenty-year integration corresponding to 7763 transits for WASP-18b, 9270 transits for WASP-19b, and 5371 transit events for WASP-77Ab. This procedure was then applied to a grid of masses and semi-major axes of the perturbing planet while fixing all the other orbital parameters. In this study, we chose to start the perturbing planet on a circular orbit that is co-planar with the transiting planet; this implies that $\Omega_2 = 0°$ and $\omega_2 = 0°$ for the perturbing and $\Omega_1 = 0°$ for the transiting planet. This setting provides a most conservative estimate of the upper mass limit of a possible perturber (Bean 2009; Fukui et al. 2011; Hoyer et al. 2011, 2012). We refer the interested reader to Wang et al. (2018c), who studied the effects of TTVs on varying initial orbital parameters.

In order to calculate the location of mean-motion resonances, we used the same code to calculate MEGNO on the same parameter grid. However, this time we integrated each initial grid point for 1000 yr, allowing this study to highlight the location of weak chaotic high-order mean-motion resonances. Briefly, MEGNO quantitatively measures the degree of stochastic behavior of a nonlinear dynamical system and has proven useful in the detection of chaotic resonances (Goździewski et al. 2001; Hinse et al. 2010). In addition to the Newtonian equations of motion, the associated variational equations of motion are solved simultaneously allowing the calculation of MEGNO at each integration time step. The MICROFARM package implements the ODEX[4] extrapolation algorithm to numerically solve the system of first-order differential equations.

Following Cincotta & Simó (2000) and Cincotta et al. (2003), the MEGNO index is defined as:

$$Y(t) = \frac{2}{T}\int_0^T \frac{\|\dot{\delta}(t)\|}{\|\delta(t)\|} t\mathrm{d}t, \tag{5}$$

where $\dot{\delta}/\delta$ is the relative change of the variational vector δ. The time-averaged or mean $Y(t)$ (time-averaged MEGNO) is given as:

$$\langle Y(t)\rangle = \frac{1}{T}\int_0^T Y(t)\mathrm{d}t. \tag{6}$$

This notation can be confusing at times. In Cincotta & Simó (2000), the MEGNO $Y(t)$ and $\langle Y(t)\rangle$ as written above are introduced as $\mathcal{J}$ and $\bar{\mathcal{J}}$, respectively. In Cincotta et al. (2003) the MEGNO index and its time-average is denoted as Y and $\bar{Y}$. When presenting results (Figs. 5–7) it is always the time-averaged MEGNO index that is used to quantitatively differentiate between quasi-periodic and chaotic dynamics. The variational vector δ is determined from an initial-value problem by numerically solving the variational equations of motion Mikkola & Innanen (1999) in parallel with the Newtonian equations of motion. We refer to Hinse et al. (2010) for a short and compact review of essential properties of MEGNO.

[2] https://bitbucket.org/chdianthus/microfarm/src
[3] https://www.open-mpi.org
[4] https://www.unige.ch/~hairer/prog/nonstiff/odex.f

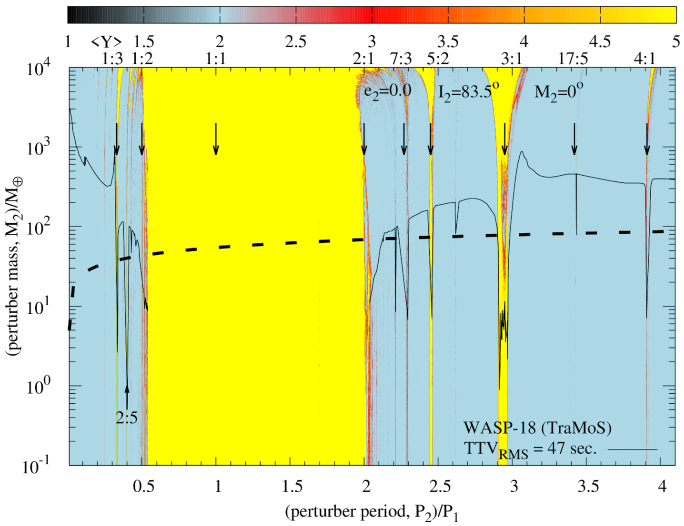

Fig. 5. MEGNO ($\langle Y\rangle$) stability map for the WASP-18 system. We overplot the map with an upper mass of a hypothetical perturbing planet introducing a mid-transit time $\mathrm{TTV_{RMS}}$ scatter of 47 s (solid line) as obtained in this study. The stipulated line is the upper mass limit as obtained from the RMS scatter (30 m s^{-1}) of the radial-velocity curve. For initial conditions resulting in aquasi-periodic (i.e., bounded) motion of the system, the $\langle Y\rangle$ value is close to 2.0 (color coded blue). For chaotic (i.e., unstable) motion, the $\langle Y\rangle$ is diverging away from 2.0 (color coded red to yellow). Vertical arrows indicate (P_2/P_1) orbital resonances between the perturbing body and the transiting planet. The two planets were assumed to be co-planar, and the eccentricity of the perturbing planet was initially set to zero.

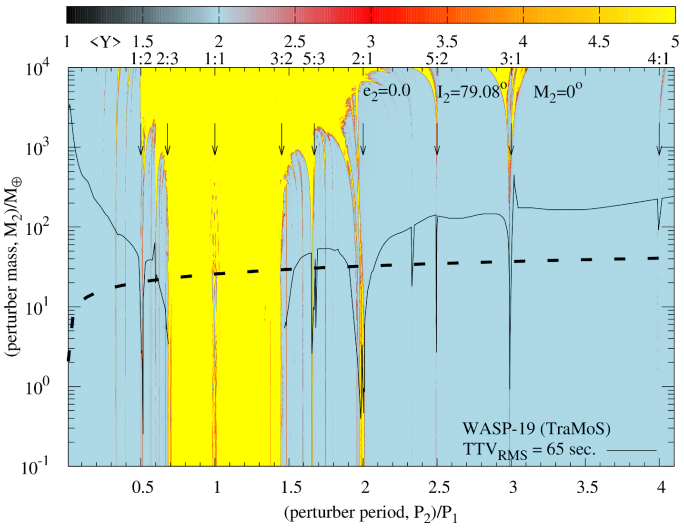

Fig. 6. Same as Fig. 5, but this time for WASP-19 with a $\mathrm{TTV_{RMS}}$ of 65 s. The RMS for the radial-velocity measurements was (18.2 m s^{-1}).

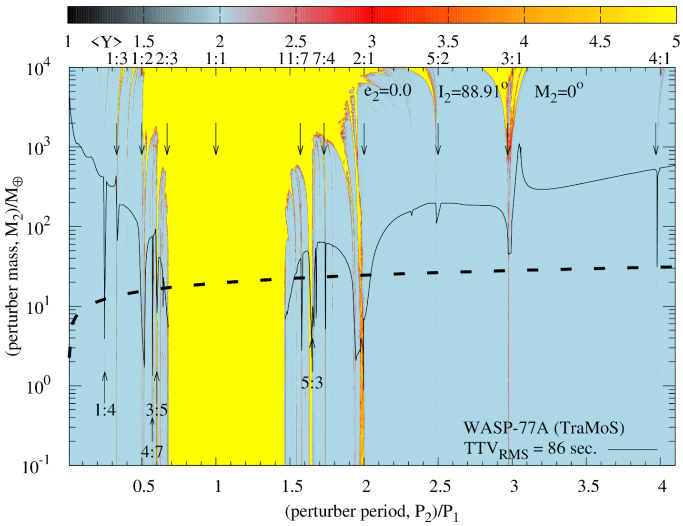

Fig. 7. Same as Fig. 5, but this time for WASP-77 with a TTV_{RMS} of 86 s. The RMS for the radial-velocity measurements was (12.0 m s^{-1}).

In a dynamical system that evolves quasi-periodically in time, the quantity $\langle Y \rangle$ will asymptotically approach 2.0 for $t \to \infty$. In that case, the orbital elements associated with that orbit are often bounded. In the case of a chaotic time evolution, the quantity $\langle Y \rangle$ diverges away from 2.0. with orbital parameters exhibiting erratic temporal excursions. For quasi-periodic orbits, we typically have $|\langle Y \rangle - 2.0| < 0.001$ at the end of each integration.

Importantly, MEGNO is unable to prove that a dynamical system is evolving quasi-periodically, meaning that a given system cannot be proven to be stable or bounded for all times. The integration of the equations of motion only considers a limited time period. However, once a given initial condition has been found to be chaotic, there is no doubt about its erratic nature in the future.

In the following, we present the results of each system for which we have calculated the RMS scatter of TTVs on a grid of the masses and semi-major axes of a perturbing planet in a circular, co-planar orbit. Results are shown in Figs. 5–7 and Table 3. In each of the three cases, we find the usual instability region located in the proximity of the transiting planet with MEGNO color-coded as yellow (corresponding to $\langle Y \rangle > 5$). The extent of these regions coincides with the results presented in Barnes & Greenberg (2006). The locations of mean-motion resonances are indicated by arrows in each map.

4.3.1. WASP-18Ab

For the WASP-18Ab system we find a large region of instability when compared to the other two systems with boundaries at the 1:2 interior and 2:1 exterior mean-motion resonance. By overplotting the RMS scatter of mid-transit times (TTV_{RMS}) for a certain value, we find that the TTVs are relatively more sensitive at orbital architectures involving mean-motion resonances confirming the results by Agol et al. (2005) and Holman & Murray (2005). This also applies to WASP-19 and WASP-77A.

As shown in Fig. 5, we find that a perturbing body of mass (upper limit) around 4–350 $M_\oplus$ will cause an RMS of 47 s when located in the P_2/P_1 = 7:3, 5:2, 3:1, 17:5 and 4:1 exterior resonance. For the 1:3 interior resonance, a perturber mass (upper limit) as small as 2.5 $M_\oplus$ could also cause a RMS mid-transit time scatter of 47 s.

Table 3. Approximate upper mass limits of a putative perturber in various orbital resonances for each system.

MMR (P_2/P_1)	WASP-18A [$M_\oplus$]	WASP-19 [$M_\oplus$]	WASP-77A [$M_\oplus$]
1:4	–	–	4.0
1:3	2.5	–	70.0 [a]
2:5	1.0	–	–
1:2	9.0 [b]	0.26	1.8
4:7	–	–	1.5
3:5	–	–	8.0
2:3	–	–	5.5 [b]
11:7	–	–	3.0
5:3	–	2.8	6.0
7:4	–	–	5.5
2:1	11.0 [b]	0.65	3.0
7:3	6.5	–	–
5:2	7.5	3.0	105.0 [c]
3:1	4.0	1.0	50.0 [d]
17:5	350.0 [e]	–	–
4:1	7.5	95.0 [f]	35.0 [g]

Notes. [a]Upper mass limit from RV: 13.4 $M_\oplus$. [b]Very close to the general instability area. [c]Upper mass limit from RV: 26.4 $M_\oplus$. [d]Upper mass limit from RV: 28.0 $M_\oplus$. [e]Upper mass limit from RV: 82.8 $M_\oplus$. [f]Upper mass limit from RV: 40.8 $M_\oplus$. [g]Upper mass limit from RV: 30.8 $M_\oplus$.

Recently, Pearson (2019) provided evidence of an additional perturber in the WASP-18A system with an orbital period of 2.155 days and an eccentricity of 0.009 ± 0.006. The mass was found to be around 50 $M_\oplus$. When comparing this with our results, the period of 2.155 days translates to a period ratio of $P_2/P_1 = 2.29$. From our dynamical analysis (see Fig. 5), this period ratio suggests an upper mass limit of 10 $M_\oplus$ for a circular orbit and implies inconsistent results. At this point, we can not offer a plausible explanation for the mass difference of a factor of five. The suggested perturber in Pearson (2019) is on a near-circular orbit which coincides with our circular case. However, the difference found is probably related to the different data set considered. While we included ground-based and TESS photometry, Pearson (2019) only analyzed TESS data.

4.3.2. WASP-19b

For the WASP-19b system, the measured transit-timing RMS scatter was TTV_{RMS} = 65s. Additional bodies with an upper mass limit as low as 0.26 $M_\oplus$ at the 1:2 (interior) mean-motion resonances could cause the observed RMS scatter. Hypothetical planets of 2.8 $M_\oplus$, 3.0 $M_\oplus$, and 1.0 $M_\oplus$ could cause the observed RMS scatter at the 5:3, 5:2, and 3:1 exterior mean-motion resonances, respectively. We refer to Fig. 6.

4.3.3. WASP-77Ab

For the WASP-77Ab system we refer to Fig. 7. The measured RMS of mid-transit timing variations around the linear ephemeris was TTV_{RMS} = 86 s. For interior mean-motion resonances of 1:2 or 2:3, the observed TTV_{RMS} could be caused by an additional planet with a mass of 1.8 $M_\oplus$ and 5.5 $M_\oplus$, respectively. However, the 2:3 resonance is very close to the general instability area rendering the orbit likely to be unstable. Further, a 70 $M_\oplus$ mass planet at the 1:3 interior resonance could also

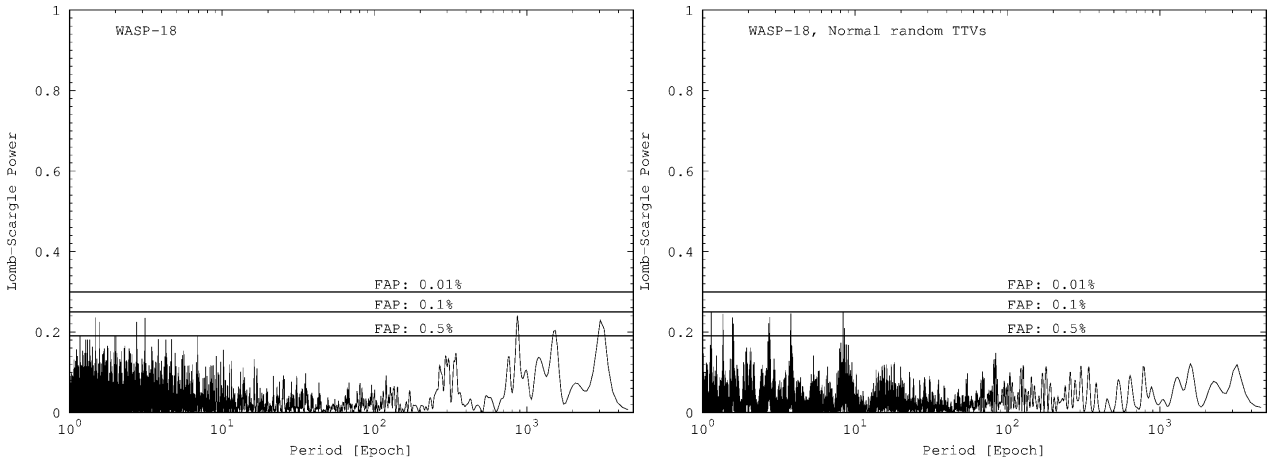

Fig. 8. Lomb-Scargle (standard normalized) power vs. period for observed TTV residuals of WASP-18A (*left panel*) and for a simulated set of TTVs randomly drawn from a normal distribution with mean zero and standard deviation of 0.78 min (*right panel*). See text for more details.

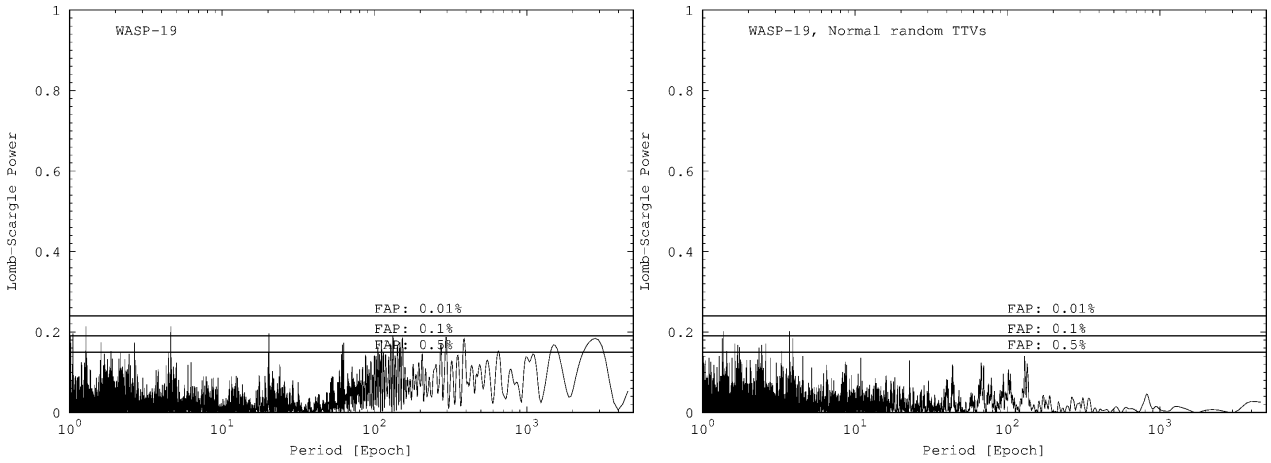

Fig. 9. Lomb-Scargle (standard normalized) power vs. period for observed TTV residuals of WASP-19 (*left panel*) and for a simulated set of TTVs randomly drawn from a normal distribution with mean zero and standard deviation of 1.08 min (*right panel*). See text for more details.

cause a $\mathrm{TTV_{RMS}}$ of 86 s. A 8 $M_\oplus$ mass planet located at the 3:5 resonance, although relatively close to the inner edge of the general instability region, could also explain the observed timing variation. For exterior mean-motion resonances of 2:1, 3:1, and 4:1 an additional planet of 3.0 $M_\oplus$, 50.0 $M_\oplus$ and 35 $M_\oplus$ in mass, respectively, could cause a $\mathrm{TTV_{RMS}}$ = 86 s.

4.4. Transit timing variation period search

We carried out a Lomb-Scargle period analysis (Lomb 1976; Scargle 1982) for the TTV residuals of each system to search for a significant periodic trend. To this end, we applied the `LombScargle`[5] (LS) algorithm available within the `Astropy` (v3.1.1) Python package (VanderPlas et al. 2012; VanderPlas & Ivezić 2015). The algorithm is suitable for unevenly sampled data. We chose to carry out computations using the observed transit epochs for each system as the independent variable. Each epoch is determined with a high degree of confidence. Measurement uncertainties on TTVs were not accounted for since no convincing periodic trends were detected. Default settings were avoided to safeguard the analysis from an inappropriate frequency grid choice. We made use of the minimum and maximum frequency heuristic. Periods of between 1 and 5000 epochs were searched for. Furthermore, we sampled each peak 12 times. Worthy of mention and often overlooked is the possible detection of frequencies much larger than the Nyquist sampling frequency (VanderPlas 2018).

The result for each system is shown in Figs. 8–10, where we show the Lomb-Scargle power P from the standard normalization method with $0 \leq P < 1$. The final period is found by multiplying with the final best-fit period for each system. To quantify the significance of period-peaks we calculated the false-alarm probability (FAP) for three different p-values. The FAP encodes the probability of detecting a peak of a given height (or higher) and is conditioned on the null-hypothesis that the data are characterized by normal random noise.

To avoid misinterpretation of the FAP we calculated synthetic random TTVs for each system in a single realization. For each known epoch, we drew a normal random point with mean zero and standard deviation in accordance with the measured RMS for each timing data set (47 s for WASP-18A, 65 s for WASP-19 and 86 s for WASP-77A).

We then recomputed the LS periodogram for each synthetic data set. This method enables a meaningful quantitative assessment of a minimum requirement of the FAP to detect a true

[5] http://docs.astropy.org/en/stable/stats/lombscargle.html

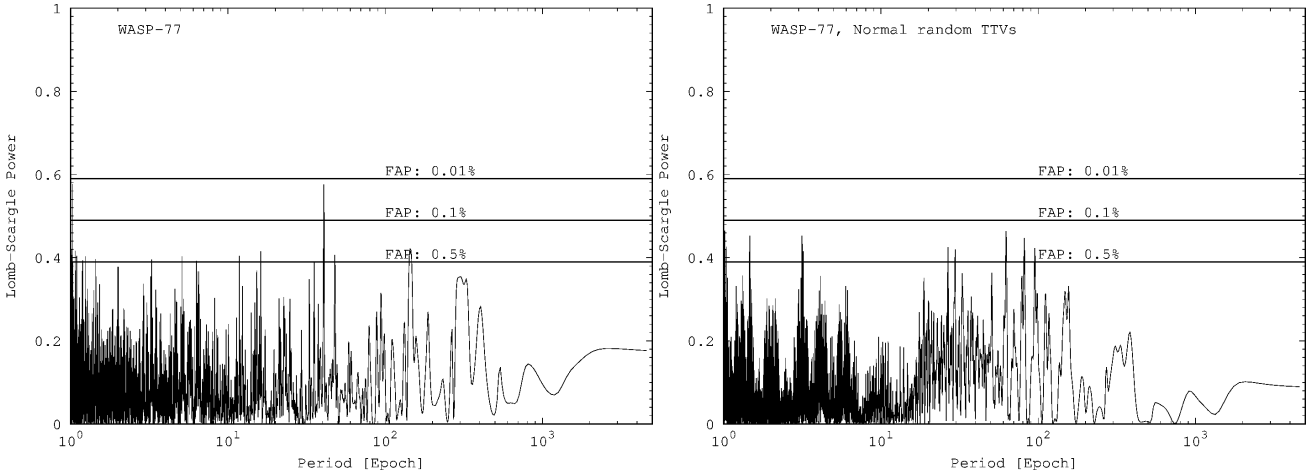

Fig. 10. Lomb-Scargle (standard normalized) power vs. period for observed TTV residuals of WASP-77A (*left panel*) and for a simulated set of TTVs randomly drawn from a normal distribution with mean zero and standard deviation of 1.43 min (*right panel*). See text for more details.

periodic signal which clearly stands out from Gaussian noise. We plot the LS periodograms for the synthetic TTVs in the right panels of Figs. 8–10. For all three systems we find that a reasonable minimum FAP of 0.1% is required in order to distinguish any true signal in our data from white noise. For all three systems, we found no significant (99.99% level) periodicity peaks with a FAP of 0.01% or smaller. The only system that exhibits a period with a FAP $\simeq$ 0.01% is WASP-77A for which a period at 40 epochs was found corresponding to $P_2 \simeq 40 \times 1.36$ days $\simeq 54$ days.

5. Summary and conclusions

We performed a photometric follow-up of the transiting exoplanets WASP-18Ab, WASP-19b, and WASP-77Ab using meter-class telescopes within the TraMoS project. Our 22 new high-precision light curves and archival data were combined to refine the physical and orbital parameters of the systems.

For WASP-18Ab we find a larger value for the fraction of the radius R_p/R_* than the most recent work with TESS data Shporer et al. (2019), and a larger total transit duration T_{14} than that of Hellier et al. (2009). The rest of the stellar and planetary parameters are all in good accordance with previous results.

In the analysis of WASP-19b, our results are in general agreement with those of previous studies (Hebb et al. 2010; Lendl et al. 2013). Only the inclination i and the total duration of the transit T_{14} show important differences.

In this work, we report the first bulk measurements of the WASP-77Ab system. We find almost no disagreement of the orbital and physical parameters with the discovery paper Maxted et al. (2013a).

We combined archival mid-transit times and new TESS light curves along with the transits from the TraMoS project to obtain refined values for the period P of the three exoplanets. We report an orbital period of $P = 0.941452417 \pm 2.7 \times 10^{-8}$ days for WASP-18Ab, $P = 0.788838940 \pm 3 \times 10^{-9}$ days for WASP-19b, and $P = 1.36002866 \pm 1.7 \times 10^{-7}$ days for WASP-77Ab. With these refined orbital periods, we propose updated linear ephemeris for the three targets. The scatter in the transit mid-time TTV_{RMS} is 47, 65, and 86 s, for WASP-18Ab, WASP-19b, and WASP-77Ab, respectively. Also, we find a lack of significant TTV periodic signals.

The TTV_{RMS} could be produced by a perturber body gravitationally bound to our targets. Therefore, we performed orbit integrations to find upper mass limits for possible companions. We found that for WASP-18Ab the observed RMS could be produced by a perturber with an upper mass limit of around 4–7.5 $M_\oplus$ in 7:3, 5:2, 3:1, and 4:1 exterior resonances, and by a body with a mass in the range of 1–11 $M_\oplus$ for the interior resonances 1:3, 1:2, 2:1, and 2:5. We compared our results with the recent submission of Pearson (2019), where evidence of a possible perturber of 50 $M_\oplus$ with an orbital period of 2.155 days is presented. However, for that period, our results place an upper mass limit of 10 $M_\oplus$.

In the case of WASP-19b, companions with upper mass limits of between 0.65 and 3 $M_\oplus$ in 2:1, 5:2, 5:3, and 3:1 exterior resonances could produce the 75 s of scatter, as well as a 0.26 $M_\oplus$ body in 1:2 interior resonance.

For WASP-77Ab, the observed RMS in the TTVs could be produced by planets with masses in the range 1.5–8 $M_\oplus$ in the interior resonances 1:2, 3:5, 2:3, 1:4, and 4:7, or by perturbing bodies with masses in the range of 3–6 $M_\oplus$ for exterior resonances 11:7, 5:3, 7:4, and 2:1.

The hypothetical perturbers with the greatest masses for the three targets are discarded because they are constrained by RV variations. These cases are: a body up to 350 $M_\oplus$ in 17:5 resonance for WASP-18Ab, 95 $M_\oplus$ in 4:1 resonance for WASP-19b, and 70 $M_\oplus$, 50 $M_\oplus$, 105 $M_\oplus$, and 35 $M_\oplus$ in 1:3 3:1, 5:2, and 4:1, resonances, respectively, for WASP-77Ab. The possible perturbers presented in this work that are not discarded by RV limits do not exceed 11 $M_\oplus$. Furthermore, we find no significant periodicity in the TTV curves of the three exoplanets by performing a Lomb-Scargle period analysis.

At this point, we find no evidence that a second-degree model is better than a linear model for WASP-18Ab. This supports the conclusion that there is no evidence for a rapid orbital decay, as proposed by Wilkins et al. (2017). Since the TTV technique is sensitive to detect tidal decays on the orbits of exoplanets, we could detect any trend in the TTV data, but we do not detect any trend. Moreover, theoretical studies (Collier Cameron & Jardine 2018) suggest a time of around 20 yr to observe a variation of 4 s in this system. Our results support that prediction.

Previous photometric studies of WASP-19b (Lendl et al. 2013; Wong et al. 2016; Petrucci et al. 2020) also suggest the lack of TTV in this system. Our results include more transit times, that is, 88 versus 56 in Wong et al. (2016) and 14 in Lendl et al. (2013), and also more recent transit light curves coming from

TESS. Finding no periodic TTV signal is consistent with their results.

This is the first detailed study of WASP-77Ab. Our results will serve as a base for future photometric and dynamic studies where an extensive follow-up should be performed. WASP-77Ab shows the largest deviation for the linear ephemeris of our targets, that is, of almost 1.5 min. More consecutive transit times are needed to understand the true nature of this planet and its possible companions.

The *Kepler* mission provided continuous photometric monitoring of thousands of stars, and ended up with the first discovery of a planetary system showing TTVs. Now TESS with its observing plan divided into sectors is delivering a large amount of photometry data especially for short-period exoplanets such as hot Jupiters. Combining the new TESS data with ground-based follow-up observations, many possible short-period TTVs could be confirmed or ruled out.

To date, none of the previous and current targets of the TraMoS project have shown TTVs (Hoyer et al. 2016, 2013, 2012). Since they are all hot Jupiters, these results suggest that these kinds of planets are probably isolated in their systems or are accompanied by small bodies, making their detection difficult. How WASP-47b (Becker et al. 2015) and Kepler-730b (Cañas et al. 2019), the only two hot Jupiters showing TTVs, have close-in companions is still unknown. Moreover, none of the current formation theories of this kind of exoplanet predict the occurrence ratio of close-in companions in their systems. However, Steffen et al. (2012a) analyzed *Kepler* data in order to constrain the occurrence rate of companions in hot Jupiter systems. In a sample of 63 candidates, none of them show evidence of close-in companions. Thus, continuing photometric follow-up investigations of hot Jupiters is crucial to unveil their planetary formation process.

Acknowledgements. The authors thank the referee for the helpful comments that improved the quality of this publication. We also acknowledge the Exoplanet Transit Database (ETD) observers: J. Gonzalez, P. Benni, D. Molina and J. Gaitan for providing us their observations of WASP-77Ab. The authors thank Ian Wong and Avi Shporer for their insights during the preparation of this paper. T.C.H. acknowledges Dr. Jennifer Burt for valuable discussion on the computation of Lomb-Scargle power spectra within PYTHON. P.C.Z. thanks the Graduate Department, Vice-Presidency of Academic Affairs of the Universidad de Chile, and Yale University for their support in the Short Term Research Programme. P.C.Z. also thanks the LSSTC Data Science Fellowship Program, which is funded by LSSTC, NSF Cybertraining Grant #1829740, the Brinson Foundation, and the Moore Foundation; her participation in the program has benefited this work. P.R. acknowledges support from CONICYT project Basal AFB-170 002. S.W. thanks Heising-Simons Foundation for their generous support.

References

Agol, E., Steffen, J., Sari, R., & Clarkson, W. 2005, MNRAS, 359, 567
Alonso, R., Brown, T. M., Charbonneau, D., et al. 2007, ASP Conf. Ser., 366, 13
Anderson, D. R., Gillon, M., Maxted, P. F. L., et al. 2010, A&A, 513, L3
Bakos, G. 2012, JAAVSO, 40, 241
Ballard, S. 2019, AJ, 157, 113
Ballard, S., Fabrycky, D., Fressin, F., et al. 2011, ApJ, 743, 200
Barnes, R., & Greenberg, R. 2006, ApJ, 647, L163
Bean, J. L. 2009, A&A, 506, 369
Bean, J. L., Désert, J.-M., Seifahrt, A., et al. 2013, ApJ, 771, 108
Becker, J. C., Vanderburg, A., Adams, F. C., Rappaport, S. A., & Schwengeler, H. M. 2015, ApJ, 812, L18
Cañas, C. I., Wang, S., Mahadevan, S., et al. 2019, ApJ, 870, L17
Cincotta, P. M., & Simó, C. 2000, A&AS, 147, 205
Cincotta, P. M., Giordano, C. M., & Simó, C. 2003, Physica D, 182, 151
Collier Cameron, A., & Jardine, M. 2018, MNRAS, 476, 2542
Csizmadia, S., Hellard, H., & Smith, A. M. S. 2019, A&A, 623, A45
Dotter, A. 2016, ApJS, 222, 8
Eastman, J. 2017, Astrophysics Source Code Library [record ascl:1710.003]
Eastman, J., Siverd, R., & Gaudi, B. S. 2010, PASP, 122, 935
Eastman, J., Gaudi, B. S., & Agol, E. 2013, PASP, 125, 83
Fabrycky, D. C., Ford, E. B., Steffen, J. H., et al. 2012, ApJ, 750, 114
Fontanive, C., Rice, K., Bonavita, M., et al. 2019, MNRAS, 485, 4967
Ford, E. B., Fabrycky, D. C., Steffen, J. H., et al. 2012, ApJ, 750, 113
Fukui, A., Narita, N., Tristram, P. J., et al. 2011, PASJ, 63, 287
Goździewski, K. 2003, A&A, 398, 315
Goździewski, K., Bois, E., Maciejewski, A. J., & Kiseleva-Eggleton, L. 2001, A&A, 378, 569
Goździewski, K., Breiter, S., & Borczyk, W. 2008, MNRAS, 383, 989
Hebb, L., Collier-Cameron, A., Triaud, A. H. M. J., et al. 2010, ApJ, 708, 224
Hellier, C., Anderson, D. R., Collier Cameron, A., et al. 2009, Nature, 460, 1098
Hinse, T. C., Christou, A. A., Alvarellos, J. L. A., & Goździewski, K. 2010, MNRAS, 404, 837
Holman, M. J., & Murray, N. W. 2005, Science, 307, 1288
Hoyer, S., López-Morales, M., Rojo, P., Minniti, D., & Adams, E. R. 2016, MNRAS, 455, 1334
Hoyer, S., Rojo, P., López-Morales, M., et al. 2011, ApJ, 733, 53
Hoyer, S., Rojo, P., & López-Morales, M. 2012, ApJ, 748, 22
Hoyer, S., López-Morales, M., Rojo, P., et al. 2013, MNRAS, 434, 46
Lendl, M., Gillon, M., Queloz, D., et al. 2013, A&A, 552, A2
Lomb, N. R. 1976, Ap&SS, 39, 447
Mackebrandt, F., Mallonn, M., Ohlert, J. M., et al. 2017, A&A, 608, A26
Mancini, L., Ciceri, S., Chen, G., et al. 2013, MNRAS, 436, 2
Mancini, L., Giordano, M., Mollière, P., et al. 2016a, MNRAS, 461, 1053
Mancini, L., Lillo-Box, J., Southworth, J., et al. 2016b, A&A, 590, A112
Maxted, P. F. L., Anderson, D. R., Collier Cameron, A., et al. 2013a, PASP, 125, 48
Maxted, P. F. L., Anderson, D. R., Doyle, A. P., et al. 2013b, MNRAS, 428, 2645
Mikkola, S., & Innanen, K. 1999, Celest. Mech. Dyn. Astron., 74, 59
Millholland, S., & Laughlin, G. 2018, ApJ, 869, L15
Miralda-Escudé, J. 2002, ApJ, 564, 1019
Nesvorný, D., & Morbidelli, A. 2008, ApJ, 688, 636
Nutzman, P. A., Fabrycky, D. C., & Fortney, J. J. 2011, ApJ, 740, L10
Pál, A., Sárneczky, K., Szabó, G. M., et al. 2011, MNRAS, 413, L43
Patra, K. C., Winn, J. N., Holman, M. J., et al. 2017, AJ, 154, 4
Pearson, K. A. 2019, AJ, 158, 243
Pepper, J., Pogge, R. W., DePoy, D. L., et al. 2007, PASP, 119, 923
Petrucci, R., Jofré, E., Gómez Maqueo Chew, Y., et al. 2020, MNRAS, 491, 1243
Poddaný, S., Brát, L., & Pejcha, O. 2010, New Astron., 15, 297
Pollacco, D. L., Skillen, I., Collier Cameron, A., et al. 2006, PASP, 118, 1407
Ricker, G. R. 2014, JAAVSO, 42, 234
Sanchis-Ojeda, R., & Winn, J. N. 2011, ApJ, 743, 61
Sanchis-Ojeda, R., Winn, J. N., & Fabrycky, D. C. 2013, Astron. Nachr., 334, 180
Scargle, J. D. 1982, ApJ, 263, 835
Sedaghati, E., Boffin, H. M. J., Csizmadia, S., et al. 2015, A&A, 576, L11
Shporer, A., Wong, I., Huang, C. X., et al. 2019, AJ, 157, 178
Southworth, J., Hinse, T. C., Jørgensen, U. G., et al. 2009, MNRAS, 396, 1023
Steffen, J. H., Ford, E. B., Rowe, J. F., et al. 2012a, ApJ, 756, 186
Steffen, J. H., Ragozzine, D., Fabrycky, D. C., et al. 2012b, Proc. Natl. Acad. Sci., 109, 7982
Szabó, R., Szabó, G. M., Dálya, G., et al. 2013, A&A, 553, A17
Torres, G., Fischer, D. A., Sozzetti, A., et al. 2012, ApJ, 757, 161
Tregloan-Reed, J., Southworth, J., & Tappert, C. 2013, MNRAS, 428, 3671
Triaud, A. H. M. J., Collier Cameron, A., Queloz, D., et al. 2010, A&A, 524, A25
Turner, J. D., Pearson, K. A., Biddle, L. I., et al. 2016, MNRAS, 459, 789
VanderPlas, J. T. 2018, ApJS, 236, 16
VanderPlas, J. T., & Ivezić, Ž. 2015, ApJ, 812, 18
VanderPlas, J., Connolly, A. J., Ivezic, Z., & Gray, A. 2012, in Proceedings of Conference on Intelligent Data Understanding (CIDU), 47
von Essen, C., Ofir, A., Dreizler, S., et al. 2018, A&A, 615, A79
Wang, S., Zhang, H., Zhou, J.-L., et al. 2014, ApJS, 211, 26
Wang, S., Wu, D.-H., Barclay, T., & Laughlin, G. P. 2017a, ApJ, submitted [arXiv:1704.04290]
Wang, Y.-H., Wang, S., Liu, H.-G., et al. 2017b, AJ, 154, 49
Wang, S., Wang, X.-Y., Wang, Y.-H., et al. 2018a, AJ, 156, 181
Wang, S., Addison, B., Fischer, D. A., et al. 2018b, AJ, 155, 70
Wang, X.-Y., Wang, S., Hinse, T. C., et al. 2018c, PASP, 130, 064401
Weinberg, N. N., Sun, M., Arras, P., & Essick, R. 2017, ApJ, 849, L11
Wilkins, A. N., Delrez, L., Barker, A. J., et al. 2017, ApJ, 836, L24
Wong, I., Knutson, H. A., Kataria, T., et al. 2016, ApJ, 823, 122
Wu, D.-H., Wang, S., Zhou, J.-L., Steffen, J. H., & Laughlin, G. 2018, AJ, 156, 96

Appendix A: Additional tables

Table A.1. System parameters of WASP-18A.

Parameter	Units	This study	Hellier et al. (2009)	Shporer et al. (2019)
Stellar parameters:				
M_*	Mass ($M_\odot$)	$1.294^{+0.063}_{-0.061}$	1.25 ± 0.13	
R_*	Radius ($R_\odot$)	$1.319^{+0.061}_{-0.062}$	$1.216^{+0.067}_{-0.054}$	
L_*	Luminosity ($L_\odot$)	$2.68^{+0.28}_{-0.26}$		
ρ_*	Density (cgs)	$0.795^{+0.11}_{-0.089}$	$0.707^{+0.056}_{-0.096}$	
$\log g$	Surface gravity (cgs)	$4.310^{+0.036}_{-0.033}$	$4.367^{+0.028}_{-0.042}$	
$T_{\rm eff}$	Effective temperature (K)	6432 ± 48	6400 ± 100	
[Fe/H]	Metallicity	0.107 ± 0.080	0.00 ± 0.09	
Age	Age (Gyr)	$1.57^{+1.4}_{-0.94}$	$0.5 - 1.5$	
Planetary parameters:				
$R_{\rm P}$	Radius (R_J)	1.240 ± 0.079	$1.106^{+0.072}_{-0.054}$	1.192 ± 0.038
$M_{\rm P}$	Mass (M_J)	10.20 ± 0.35	10.30 ± 0.69	
P	Period (days)	$0.94145223 \pm (24)$ [b]	$0.94145299 \pm (87)$ [b]	$0.9414576^{(+34)}_{(-35)}$ [b]
e	Eccentricity	$0.0051^{+0.0070}_{-0.0037}$	0.0092 ± 0.0028	
a	Semi-major axis (AU)	$0.02024^{+0.00029}_{-0.00031}$	0.02045 ± 0.00067	
ω_*	Argument of Periastron (degrees)	-85^{+72}_{-96}		
$\rho_{\rm P}$	Density (cgs)	$6.6^{+1.2}_{-1.1}$	$7.73^{+0.78}_{-1.27}$ [a]	
$\log g_{\rm P}$	Surface gravity	$4.215^{+0.046}_{-0.052}$	$4.289^{+0.027}_{-0.050}$	
$T_{\rm eq}$	Equilibrium temperature (K)	2429^{+77}_{-70}	2384^{+58}_{-30}	
Θ	Safronov number	$0.268^{+0.016}_{-0.017}$		
$\langle F \rangle$	Incident flux (10^9 erg s^{-1} cm^{-2})	$7.90^{+1.10}_{-0.87}$		
Primary transit parameters:				
T_0	Transit time (BJD$_{\rm TDB}$)	$2456740.80560 \pm (19)$ [b]	$2454221.48163 \pm (38)$ [b]	$2458361.048072^{(+34)}_{(-35)}$ [b]
i	Inclination (degrees)	$83.5^{+2.0}_{-1.6}$	86.0 ± 2.5	$84.31^{+0.40}_{-0.37}$
$R_{\rm P}/R_*$	Radius of planet in stellar radii	0.1018 ± 0.0011	0.0935 ± 0.0011	$0.09721^{+0.00016}_{-0.00017}$
a/R_*	Semi-major axis in stellar radii	$3.48^{+0.16}_{-0.17}$		$3.523^{+0.028}_{-0.027}$
b	Impact parameter	$0.36^{+0.11}_{-0.18}$	0.25 ± 0.15	$0.349^{+0.020}_{-0.022}$
δ	Transit depth (fraction)	0.01041 ± 0.00022		$0.009449^{+0.000032}_{-0.000032}$
$u_{1,I}$	Linear LD coeff., I band	0.207 ± 0.019		
$u_{2,I}$	Quadratic LD coeff., I band	0.313 ± 0.019		
$u_{1,R}$	Linear LD coeff., R band	0.257 ± 0.045		
$u_{2,\rm R}$	Quadratic LD coeff., R band	0.309 ± 0.048		
T_{14}	Total transit duration (days)	$0.0921^{+0.0013}_{-0.0011}$	0.08932 ± 0.00068	
$P_{\rm T}$	A priori non-grazing transit prob	$0.258^{+0.014}_{-0.011}$		
$P_{\rm T,G}$	A priori transit prob	$0.316^{+0.017}_{-0.014}$		
τ	Ingress/egress transit duration (days)	0.0099 ± 0.0012		
RV parameters:				
$e \cos \omega_*$		$0.0002^{+0.0033}_{-0.0028}$		
$e \sin \omega_*$		$-0.0022^{+0.0039}_{-0.0079}$		
K	RV semi-amplitude (m s^{-1})	1814^{+23}_{-24}	1818.3 ± 8.0	
$M_{\rm P} \sin i$	Minimum mass (M_J)	10.14 ± 0.33		
Secondary eclipse parameters:				
$T_{\rm S}$	Time of eclipse (BJD$_{\rm TDB}$)	$2457657.3119^{+0.0021}_{-0.0019}$		
$b_{\rm S}$	Eclipse impact parameter	$0.35^{+0.11}_{-0.17}$		
$\tau_{\rm S}$	Ingress/egress eclipse duration (days)	$0.0098^{+0.0013}_{-0.0010}$		
$T_{\rm S,14}$	Total eclipse duration (days)	0.0917 ± 0.0016		
$P_{\rm S}$	A priori non-grazing eclipse prob	$0.259^{+0.013}_{-0.012}$		
$P_{\rm S,G}$	A priori eclipse prob	$0.318^{+0.017}_{-0.015}$		

Notes. Value converted to cgs units multiplying by the Sun density $\rho_\odot = 1.408$ cgs. [a]Value converted to cgs units multiplying by the Jupiter density $\rho_J = 1.33$ cgs. [b]Values enclosed in parentheses correspond to the uncertainties of the last digits of the nominal value.

Table A.2. System parameter of WASP-19.

Parameter	Units	This study	Hebb et al. (2010) [a]	Lendl et al. (2013)
Stellar parameters:				
M_*	Mass ($M_\odot$)	$0.965^{+0.091}_{-0.095}$	0.95 ± 0.10	$0.968^{+0.084}_{-0.079}$
R_*	Radius ($R_\odot$)	$1.006^{+0.031}_{-0.034}$	$0.93^{+0.05}_{-0.04}$	0.994 ± 0.031
L_*	Luminosity ($L_\odot$)	$0.905^{+0.071}_{-0.069}$		
ρ_*	Density (cgs)	$1.339^{+0.056}_{-0.058}$	$1.19^{+0.12}_{-0.11}$ [b]	$1.384^{+0.055}_{-0.051}$ [b]
$\log g$	Surface gravity (cgs)	$4.417^{+0.020}_{-0.021}$	4.48 ± 0.03	
$T_{\rm eff}$	Effective temperature (K)	5616^{+66}_{-65}	5500 ± 100	
[Fe/H]	Metallicity	$0.04^{+0.25}_{-0.30}$	0.02 ± 0.09	
Age	Age (Gyr)	$6.4^{+4.1}_{-3.5}$	$5.5^{+9.0}_{-4.5}$	
Planetary parameters:				
$R_{\rm P}$	Radius (R_J)	$1.415^{+0.044}_{-0.048}$	1.28 ± 0.07	1.376 ± 0.046
$M_{\rm P}$	Mass (M_J)	$1.154^{+0.078}_{-0.080}$	1.14 ± 0.07	1.165 ± 0.068
P	Period (days)	$0.78883852^{+(75)}_{-(82)}$ [d]	$0.7888399 \pm (8)$ [d]	$0.7888390 \pm (2)$ [d]
e	Eccentricity	$0.0126^{+0.014}_{-0.0089}$		$0.0077^{+0.0068}_{-0.0032}$
a	Semi-major axis (AU)	$0.01652^{+0.00050}_{-0.00056}$	$0.0164^{+0.0005}_{-0.0006}$	0.01653 ± 0.00046
ω_*	Argument of periastron (degrees)	51^{+89}_{-190}	-76^{+112}_{-23}	43^{+28}_{-67}
$\rho_{\rm P}$	Density (cgs)	$0.506^{+0.031}_{-0.030}$	$0.54^{+0.07}_{-0.06}$	$0.595^{+0.036}_{-0.033}$ [c]
$\log g_{\rm P}$	Surface gravity	$3.155^{+0.018}_{-0.019}$	3.20 ± 0.03	3.184 ± 0.015
$T_{\rm eq}$	Equilibrium temperature (K)	2113 ± 29	1993^{+32}_{-33}	2058 ± 40
Θ	Safronov number	$0.0279^{+0.0012}_{-0.0011}$		
$\langle F \rangle$	Incident flux (10^9 erg s^{-1} cm^{-2})	$4.52^{+0.26}_{-0.24}$		
Primary transit parameters:				
T_0	Transit time ($\rm BJD_{TDB}$)	$2456402.7128^{+(17)}_{-(14)}$	$2454775.3372 \pm (2)$	$2456029.59204 \pm (13)$
i	Inclination (degrees)	$79.08^{+0.34}_{-0.37}$	80.8 ± 0.8	79.54 ± 0.33
$R_{\rm P}/R_*$	Radius of planet in stellar radii	$0.14410^{+0.00049}_{-0.00050}$	0.1425 ± 0.0014	
a/R_*	Semi-major axis in stellar radii	$3.533^{+0.048}_{-0.052}$		3.573 ± 0.046
b	Impact parameter	$0.6671^{+0.0087}_{-0.0091}$	0.62 ± 0.03	0.645 ± 0.012
δ	Transit depth (fraction)	0.02077 ± 0.00014	0.0203 ± 0.0004	0.02018 ± 0.00021
$u_{1,\rm I}$	linear LD coeff., I band	$0.287^{+0.027}_{-0.029}$		
$u_{2,\rm I}$	Quadratic LD coeff., I band	0.263 ± 0.024		
$u_{1,\rm R}$	Linear LD coeff., R band	$0.383^{+0.029}_{-0.032}$		
$u_{2,\rm R}$	Quadratic LD coeff., R band	$0.246^{+0.027}_{-0.025}$		
T_{14}	Total transit duration (days)	$0.06697^{+0.00031}_{-0.00030}$	$0.0643^{+0.0006}_{-0.0007}$	$0.06586^{+0.00033}_{-0.00031}$
$P_{\rm T}$	A priori non-grazing transit prob	$0.2426^{+0.0066}_{-0.0051}$		
$P_{\rm T,G}$	A priori transit prob	$0.3246^{+0.0089}_{-0.0069}$		
τ	Ingress/egress transit duration (days)	0.01459 ± 0.00035		
RV parameters:				
$e \cos \omega_*$		$-0.0027^{+0.0077}_{-0.013}$	0.004 ± 0.009	0.0024 ± 0.0020
$e \sin \omega_*$		$0.0016^{+0.014}_{-0.0092}$	-0.02 ± 0.02	0.000 ± 0.005
K	RV semi-amplitude (m s^{-1})	$255.4^{+6.1}_{-6.2}$	256 ± 5	257.7 ± 2.9
$M_{\rm P} \sin i$	Minimum mass (M_J)	$1.133^{+0.078}_{-0.079}$		
Secondary eclipse parameters:				
$T_{\rm S}$	Time of eclipse ($\rm BJD_{TDB}$)	$2455169.3621^{+(41)}_{-(51)}$ [d]	$2456030.77766 \pm (88)$ [d]	
$b_{\rm S}$	Eclipse impact parameter	$0.670^{+0.020}_{-0.017}$	0.652 ± 0.015	
$\tau_{\rm S}$	Ingress/egress eclipse duration (days)	$0.01472^{+0.00085}_{-0.00066}$		
$T_{\rm S,14}$	Total eclipse duration (days)	$0.06812^{+0.00087}_{-0.00074}$		
$P_{\rm S}$	A priori non-grazing eclipse prob	0.2415 ± 0.0021		
$P_{\rm S,G}$	A priori eclipse prob	0.3232 ± 0.0030		

Notes. [a]For comparison, the results from Hellier et al. (2009) that considered free eccentricity were used. [b]Values converted to cgs units multiplying by the Sun density $\rho_\odot = 1.408$ cgs. [c]Values converted to cgs units multiplying by the Jupiter density $\rho_J = 1.33$ cgs. [d]Values enclosed in parentheses correspond to the uncertainties of the last digits of the nominal value.

Table A.3. System parameters of WASP-77A.

Parameter	Units	This study	Maxted et al. (2013a)
Stellar parameters:			
M_*	Mass ($M_\odot$)	$0.903^{+0.066}_{-0.059}$	1.002 ± 0.045
R_*	Radius ($R_\odot$)	$0.910^{+0.025}_{-0.023}$	0.955 ± 0.015
L_*	Luminosity ($L_\odot$)	$0.743^{+0.065}_{-0.058}$	
ρ_*	Density (cgs)	$1.692^{+0.056}_{-0.069}$ [a]	$1.629^{+0.023}_{-0.028}$ [a]
$\log g$	Surface gravity (cgs)	$4.476^{+0.014}_{-0.015}$	4.33 ± 0.08
$T_{\rm eff}$	Effective temperature (K)	5617 ± 72	5500 ± 80
[Fe/H]	Metallicity	$-0.10^{+0.10}_{-0.11}$	0.00 ± 0.11
Age	Age (Gyr)	$6.2^{+4.0}_{-3.5}$	$0.5 - 1.0$
Planetary Parameters:			
$R_{\rm P}$	Radius (R_J)	$1.230^{+0.031}_{-0.029}$	1.21 ± 0.02
$M_{\rm P}$	Mass (M_J)	$1.667^{+0.068}_{-0.064}$	1.76 ± 0.06
P	Period (days)	$1.36002854 \pm (62)$ [c]	$1.3600309 \pm (20)$ [c]
e	Eccentricity	$0.0074^{+0.0069}_{-0.0049}$	
a	Semi-major axis (AU)	$0.02335^{+0.00045}_{-0.00043}$	0.0240 ± 0.00036
ω_*	Argument of periastron (degrees)	-166^{+66}_{-75}	
$\rho_{\rm P}$	Density (cgs)	$1.115^{+0.052}_{-0.062}$	1.33 ± 0.04 [b]
$\log g_{\rm P}$	Surface gravity	$3.438^{+0.012}_{-0.016}$	3.441 ± 0.008
$T_{\rm eq}$	Equilibrium temperature (K)	1715^{+26}_{-25}	
Θ	Safronov number	0.0689 ± 0.0018	
$\langle F \rangle$	Incident Flux (10^9 erg s^{-1} cm^{-2})	$1.96^{+0.12}_{-0.11}$	
Primary Transit Parameters:			
T_0	Transit time (BJD$_{\rm TDB}$)	$2457420.88439^{(+80)}_{(-85)}$ [c]	$2455870.44977 \pm (20)$ [c]
i	Inclination (degrees)	$88.91^{+0.74}_{-0.95}$	$89.4^{+0.4}_{-0.7}$
$R_{\rm P}/R_*$	Radius of planet in stellar radii	$0.13354^{+0.00074}_{-0.00070}$	
a/R_*	Semi-major axis in stellar radii	$5.332^{+0.057}_{-0.081}$	
b	Impact parameter	$0.109^{+0.089}_{-0.071}$	$0.06^{+0.07}_{-0.05}$
δ	Transit depth (fraction)	$0.01783^{+0.00020}_{-0.00019}$	
$u_{1,\rm B}$	linear LD coeff., B band	0.680 ± 0.054	
$u_{2,B}$	quadratic LD coeff., B band	$0.140^{+0.052}_{-0.053}$	
$u_{1,\rm clear}$	linear LD coeff., clear band	0.386 ± 0.029	
$u_{2,\rm clear}$	quadratic LD coeff., clear band	0.227 ± 0.029	
$u_{1,I}$	linear LD coeff., I band	0.311 ± 0.025	
$u_{2,I}$	quadratic LD coeff., I band	0.294 ± 0.033	
$u_{1,\rm R}$	linear LD coeff., R band	0.312 ± 0.023	
$u_{2,\rm R}$	quadratic LD coeff., R band	$0.237^{+0.029}_{-0.028}$	
T_{14}	Total transit duration (days)	$0.08952^{+0.00053}_{-0.00051}$	
$P_{\rm T}$	A priori non-grazing transit prob	$0.1578^{+0.0029}_{-0.0025}$	
$P_{\rm T,G}$	A priori transit prob	$0.2064^{+0.0039}_{-0.0033}$	
τ	Ingress/egress transit duration (days)	$0.01075^{+0.00032}_{-0.00015}$	
RV parameters:			
$e \cos \omega_*$		$-0.0039^{+0.0041}_{-0.0051}$	
$e \sin \omega_*$		$-0.0003^{+0.0061}_{-0.0076}$	
K	RV semi-amplitude (m/s)	$323.4^{+3.8}_{-3.4}$	321.9 ± 3.9
$M_{\rm P} \sin i$	Minimum mass (M_J)	$1.667^{+0.068}_{-0.064}$	
Secondary eclipse parameters:			
$T_{\rm S}$	Time of eclipse (BJD$_{\rm TDB}$)	$2457658.2054^{+0.0036}_{-0.0044}$	
$b_{\rm S}$	Eclipse impact parameter	$0.109^{+0.092}_{-0.081}$	
τ_S	Ingress/egress eclipse duration (days)	$0.01116^{+0.00041}_{-0.00025}$	
$T_{\rm S,14}$	Total eclipse duration (days)	$0.0922^{+0.0012}_{-0.0014}$	
$P_{\rm S}$	A priori non-grazing eclipse prob	$0.1624^{+0.0022}_{-0.0012}$	
$P_{\rm S,G}$	A priori eclipse prob	$0.2126^{+0.0031}_{-0.0015}$	

Notes. [a]Value converted to cgs units multiplying by the Sun density $\rho_\odot = 1.408$ cgs. [b]Value converted to cgs units multiplying by the Jupiter density $\rho_J = 1.33$ cgs. [c]Values enclosed in parentheses correspond to the uncertainties of the last digits of the nominal value.

Table A.4. Transit mid-times of WASP-18Ab.

Epoch	Transit mid-time (BJD_{TDB})	TTV (min)	Reference
−2873	2 454 221.48238	0.1 ± 1.5	Hellier et al. (2009)
−2402	2 454 664.9061	−0.4 ± 1.4	Triaud et al. (2010)
−1904	2 455 133.7472	−3.4 ± 1.7	TraMoS
−1903	2 455 134.6914	0.6 ± 1.7	TraMoS
−1902	2 455 135.6331	0.9 ± 1.7	TraMoS
−1811	2 455 221.3042	−0.6 ± 1.4	Maxted et al. (2013a)
−1629	2 455 392.6474	−2.2 ± 1.5	Maxted et al. (2013a)
−1601	2 455 419.0083	−1.8 ± 2.2	Maxted et al. (2013a)
−1587	2 455 432.1897	−0.3 ± 1.4	Maxted et al. (2013a)
−1546	2 455 470.7885	−1.4 ± 1.4	Maxted et al. (2013a)
−1543	2 455 473.6144	0.9 ± 1.9	Maxted et al. (2013a)
−1457	2 455 554.5786	−0.2 ± 1.5	Maxted et al. (2013a)
−1440	2 455 570.5842	1.2 ± 1.6	Maxted et al. (2013a)
−1184	2 455 811.5970	2.7 ± 5.9	TraMoS
−1115	2 455 876.5559	0.8 ± 2.3	Maxted et al. (2013a)
776	2 457 656.84078	−1.1 ± 1.4	TraMoS
777	2 457 657.78359	0.9 ± 1.4	TraMoS
778	2 457 658.72404	−0.6 ± 1.4	TraMoS
1169	2 458 026.83186	−0.6 ± 1.5	TraMoS
1518	2 458 355.39936	0.1 ± 0.9	TESS
1519	2 458 356.34074	0.0 ± 0.9	TESS
1520	2 458 357.28226	0.1 ± 0.9	TESS
1521	2 458 358.22348	−0.3 ± 0.9	TESS
1522	2 458 359.16512	0.0 ± 0.9	TESS
1523	2 458 360.10663	0.1 ± 0.9	TESS
1524	2 458 361.04812	0.1 ± 0.9	TESS
1525	2 458 361.98970	0.3 ± 0.9	TESS
1526	2 458 362.93130	0.5 ± 0.9	TESS
1527	2 458 363.87265	0.4 ± 0.9	TESS
1528	2 458 364.81372	−0.2 ± 0.9	TESS
1529	2 458 365.75526	0.0 ± 0.9	TESS
1530	2 458 366.69705	0.5 ± 0.9	TESS
1533	2 458 369.52129	0.3 ± 0.9	TESS
1534	2 458 370.46287	0.5 ± 0.9	TESS
1535	2 458 371.40404	0.1 ± 0.9	TESS
1536	2 458 372.34538	−0.1 ± 0.9	TESS
1537	2 458 373.28724	0.5 ± 0.9	TESS
1538	2 458 374.22817	−0.3 ± 0.9	TESS
1539	2 458 375.16977	0.0 ± 0.9	TESS
1540	2 458 376.11119	−0.1 ± 0.9	TESS
1541	2 458 377.05269	0.0 ± 0.9	TESS
1542	2 458 377.99449	0.5 ± 0.9	TESS
1543	2 458 378.93575	0.2 ± 0.9	TESS
1544	2 458 379.87717	0.2 ± 0.9	TESS
1551	2 458 386.46725	0.0 ± 0.9	TESS
1552	2 458 387.40886	0.3 ± 0.9	TESS
1553	2 458 388.35016	0.0 ± 0.9	TESS
1554	2 458 389.29158	0.0 ± 0.9	TESS
1555	2 458 390.23338	0.5 ± 0.9	TESS
1556	2 458 391.17453	0.1 ± 0.9	TESS
1557	2 458 392.11596	0.0 ± 0.9	TESS
1558	2 458 393.05747	0.1 ± 0.9	TESS
1559	2 458 393.99900	0.2 ± 0.9	TESS
1560	2 458 394.94027	0.0 ± 0.9	TESS
1562	2 458 396.82304	−0.2 ± 0.9	TESS
1563	2 458 397.76450	−0.2 ± 0.9	TESS
1564	2 458 398.70659	0.7 ± 0.9	TESS
1565	2 458 399.64752	−0.1 ± 0.9	TESS
1566	2 458 400.58902	0.0 ± 0.9	TESS
1567	2 458 401.53081	0.5 ± 0.9	TESS
1568	2 458 402.47199	0.1 ± 0.9	TESS
1569	2 458 403.41362	0.4 ± 0.9	TESS
1570	2 458 404.35477	−0.1 ± 0.9	TESS
1571	2 458 405.29598	−0.4 ± 0.9	TESS

Table A.5. Transit mid-times of WASP-19b.

Epoch	Transit mid-time (BJD_{TDB})	TTV (min)	Reference
−2063	2 454 775.3372	−1.6 ± 3.2	Hebb et al. (2010)
−2061	2 454 776.91566	−0.5 ± 2.3	Anderson et al. (2010)
−2010	2 454 817.14633	−0.6 ± 2.3	Lendl et al. (2013)
−1525	2 455 199.73343	−0.2 ± 2.6	Exoplanet Transit Database
−1459	2 455 251.79657	−0.6 ± 2.3	Tregloan-Reed et al. (2013)
−1458	2 455 252.58544	−0.5 ± 2.3	Tregloan-Reed et al. (2013)
−1454	2 455 255.74077	−0.6 ± 2.3	Tregloan-Reed et al. (2013)
−1449	2 455 259.68448	−1.3 ± 2.4	Exoplanet Transit Database
−1431	2 455 273.88282	−2.4 ± 2.5	Exoplanet Transit Database
−1399	2 455 299.12768	0.6 ± 2.4	Exoplanet Transit Database
−1354	2 455 334.6254	0.5 ± 2.3	Mancini et al. (2013)
−1349	2 455 338.56927	0.1 ± 2.3	Lendl et al. (2013)
−1330	2 455 353.55659	−0.8 ± 2.3	Mancini et al. (2013)
−1317	2 455 363.81131	−1.1 ± 2.4	Exoplanet Transit Database
−1311	2 455 368.54285	−3.3 ± 3.8	Mancini et al. (2013)
−1094	2 455 539.72327	0.2 ± 2.4	Lendl et al. (2013)
−1056	2 455 569.69826	−1.1 ± 2.4	Lendl et al. (2013)
−1039	2 455 583.10979	0.8 ± 2.6	Exoplanet Transit Database
−1037	2 455 584.68693	0.0 ± 2.3	Lendl et al. (2013)
−1025	2 455 594.15188	−1.6 ± 3.3	Mancini et al. (2013)
−1016	2 455 601.25164	−1.3 ± 2.5	Mancini et al. (2013)
−1014	2 455 602.83138	1.7 ± 2.4	Lendl et al. (2013)
−1011	2 455 605.19414	−3.8 ± 3.5	Mancini et al. (2013)
−1009	2 455 606.77464	0.3 ± 2.3	Lendl et al. (2013)
−1008	2 455 607.56241	−1.2 ± 2.4	Lendl et al. (2013)
−989	2 455 622.55057	−0.9 ± 2.3	Lendl et al. (2013)
−987	2 455 624.12787	−1.5 ± 3.1	Mancini et al. (2013)
−976	2 455 632.80612	0.0 ± 2.3	Lendl et al. (2013)
−947	2 455 655.68222	−0.3 ± 2.4	Lendl et al. (2013)
−928	2 455 670.66976	−0.9 ± 2.5	Lendl et al. (2013)
−923	2 455 674.61367	−1.3 ± 2.4	TraMoS
−919	2 455 677.77038	0.7 ± 3.6	Mancini et al. (2013)
−905	2 455 688.81201	−2.4 ± 5.3	Mancini et al. (2013)
−904	2 455 689.60276	0.4 ± 2.4	Mancini et al. (2013)
−900	2 455 692.75674	−1.6 ± 4.3	Mancini et al. (2013)
−899	2 455 693.54639	−0.5 ± 2.3	Mancini et al. (2013)
−886	2 455 703.79933	−3.3 ± 6.4	Mancini et al. (2013)
−885	2 455 704.59078	0.5 ± 2.4	Mancini et al. (2013)
−880	2 455 708.534626	0.0 ± 2.3	Mancini et al. (2013)
−654	2 455 886.81234	0.2 ± 3.8	Mancini et al. (2013)
−642	2 455 896.27611	−3.1 ± 3.8	Mancini et al. (2013)
−618	2 455 915.20980	−0.9 ± 2.5	Mancini et al. (2013)
−613	2 455 919.15485	0.4 ± 2.7	Mancini et al. (2013)
−611	2 455 920.7353	0.0 ± 5.4	TraMoS
−609	2 455 922.30966	−0.4 ± 8.3	Mancini et al. (2013)
−511	2 455 999.6163	0.2 ± 2.3	Bean et al. (2013)
−483	2 456 021.70374	0.1 ± 2.3	Bean et al. (2013)
−473	2 456 029.5925	0.7 ± 2.4	Lendl et al. (2013)
−468	2 456 033.53643	0.3 ± 2.3	Mancini et al. (2013)
−430	2 456 063.51174	−0.5 ± 2.3	Lendl et al. (2013)
−86	2 456 334.87208	−0.8 ± 2.4	Exoplanet Transit Database
−47	2 456 365.6373	−0.1 ± 2.3	TraMoS
1	2 456 403.50158	−0.1 ± 2.3	TraMoS
729	2 456 977.77722	1.3 ± 2.3	Sedaghati et al. (2015)
867	2 457 086.63571	−0.5 ± 2.3	TraMoS
1383	2 457 493.67676	−0.2 ± 2.3	TraMoS
1771	2 457 799.74612	−0.3 ± 2.3	TraMoS
1838	2 457 852.597807	−0.7 ± 2.3	TraMoS
2064	2 458 030.8751	−1.5 ± 3.2	TraMoS
2716	2 458 545.19919	−0.3 ± 1.0	TESS
2717	2 458 545.98937	1.7 ± 1.0	TESS
2718	2 458 546.77766	0.9 ± 1.0	TESS
2719	2 458 547.56690	1.5 ± 1.1	TESS
2720	2 458 548.35441	−0.4 ± 1.0	TESS
2721	2 458 549.14447	1.3 ± 1.0	TESS

Table A.5. continued.

Epoch	Transit mid-time (BJD_{TDB})	TTV (min)	Reference
2722	2 458 549.93234	−0.1 ± 1.0	TESS
2723	2 458 550.72134	0.2 ± 1.0	TESS
2724	2 458 551.50995	−0.2 ± 1.0	TESS
2725	2 458 552.29885	−0.1 ± 1.0	TESS
2726	2 458 553.08808	0.5 ± 1.0	TESS
2727	2 458 553.87683	0.4 ± 0.9	TESS
2728	2 458 554.66545	0.0 ± 1.0	TESS
2729	2 458 555.45414	−0.2 ± 1.0	TESS
2732	2 458 557.82191	1.6 ± 1.0	TESS
2733	2 458 558.60961	0.0 ± 1.0	TESS
2734	2 458 559.39918	1.0 ± 1.0	TESS
2735	2 458 560.18695	−0.5 ± 1.0	TESS
2736	2 458 560.97701	1.3 ± 1.0	TESS
2737	2 458 561.76565	1.0 ± 1.0	TESS
2738	2 458 562.55360	−0.3 ± 1.0	TESS
2739	2 458 563.34290	0.4 ± 1.0	TESS
2740	2 458 564.13196	0.7 ± 0.9	TESS
2741	2 458 564.92117	1.2 ± 1.0	TESS
2742	2 458 565.70927	0.1 ± 1.0	TESS
2743	2 458 566.49876	1.1 ± 0.9	TESS
2744	2 458 567.28769	1.2 ± 1.0	TESS
2745	2 458 568.07643	1.0 ± 1.0	TESS

Table A.6. Transit mid-times of WASP-77Ab.

Epoch	Transit mid-time (BJD_{TDB})	TTV (min)	Reference
−1140	2 455 870.45054	−2.0 ± 1.5	Maxted et al. (2013a)
−845	2 456 271.65888	−2.0 ± 1.4	Turner et al. (2016)
−659	2 456 524.62617	0.8 ± 1.8	Exoplanet Transit Database
−606	2 456 596.70591	−1.7 ± 1.5	Exoplanet Transit Database
−92	2 457 295.7626	1.2 ± 1.3	TraMoS
−89	2 457 299.84119	−1.0 ± 1.3	TraMoS
175	2 457 658.88744	−2.8 ± 1.5	TraMoS
177	2 457 661.60987	0.6 ± 1.7	Exoplanet Transit Database
183	2 457 669.77054	1.4 ± 1.4	TraMoS
229	2 457 732.33382	4.2 ± 1.4	Exoplanet Transit Database
447	2 458 028.8159	−1.8 ± 6.5	TraMoS
728	2 458 410.98440	−1.2 ± 1.3	TESS
729	2 458 412.34460	−1.0 ± 1.3	TESS
730	2 458 413.70531	0.0 ± 1.3	TESS
731	2 458 415.06491	−0.6 ± 1.3	TESS
732	2 458 416.42497	−0.6 ± 1.3	TESS
733	2 458 417.78493	−0.7 ± 1.3	TESS
736	2 458 421.86480	−1.0 ± 1.3	TESS
739	2 458 425.94511	−0.7 ± 1.3	TESS
740	2 458 427.30511	−0.7 ± 1.3	TESS
741	2 458 428.66460	−1.5 ± 1.3	TESS
742	2 458 430.02488	−1.1 ± 1.3	TESS
743	2 458 431.38494	−1.1 ± 1.3	TESS
744	2 458 432.74541	−0.4 ± 1.3	TESS
745	2 458 434.10526	−0.7 ± 1.3	TESS
746	2 458 435.46538	−0.6 ± 1.3	TESS